Preliminary estimation of the detection possibilities of Ganymede's water vapor environment with MAJIS

Christina Plainaki (1), Giuseppe Sindoni (1), Davide Grassi (2), Luigi Cafarelli (1)(3), Emiliano D'Aversa (2), Stefano Massetti (2), Alessandro Mura (2), Anna Milillo (2), Gianrico Filacchione (2), Giuseppe Piccioni (2), Yves Langevin (4), Francois Poulet (4), Federico Tosi (2), Alessandra Migliorini (2), Francesca Altieri (2)

(1) Italian Space Agency, Rome, Italy (christina.plainaki@asi.it)

(2) INAF - Institute of Space Astrophysics and Planetology, Rome, Italy

(3) University of Tor Vergata, Rome, Italy

(4) Institut d'Astrophysique Spatiale, Orsay, France.

Abstract

The exosphere of Ganymede is the interface region linking the moon's icy surface to Jupiter's magnetospheric environment. Its characterization is of key importance to achieve a full understanding of the ice alteration processes induced by the radiation environment. Several scientific instruments that will operate on board the upcoming Jupiter Icy Moons Explorer (JUICE) mission, selected by ESA in the context of its Cosmic Vision programme, have the potential to study Ganymede's exosphere. Among them, the Moons And Jupiter Imaging Spectrometer (MAJIS) will have the chance to investigate the composition of the moon's exospheric components and the emission of water molecules. The exospheric water density profile, as obtained from current models, is a crucial parameter for the estimation of the expected signal to noise ratio related to the actual measurement. In lack of an adequate number of Ganymede's observations from past missions, there is a general

difficulty in constraining current exosphere models which are based, in general, on different scenarios and considerations and often show large discrepancies in the estimated spatial distribution of the neutral environment. In this work, we make a preliminary estimation of the expected IR emission from exospheric water molecules, using different modelled density profiles, and we speculate on the possibility of JUICE/MAJIS to detect it. An exercise on the potential plume detection capabilities of MAJIS is also performed. The first necessary step for performing these calculations is a rough comparison of the existing models of Ganymede's water vapor exosphere. We discuss the characteristics of the neutral environment as derived from different exospheric models available in literature, the role of the ion-surface interactions in the H_2O exosphere generation, and the related implications also in view of future observations. We then use the model outputs to estimate different scenarios for the expected non-Local Thermal Equilibrium (non-LTE) emission from these molecules. The results of this study can be of help during the JUICE observation planning phase.

1. Introduction: general concept and motivation for the current work

Ganymede is the only known moon in the Solar System so far explored to possess an intrinsic magnetic field embedded within a planetary magnetosphere (Gurnett et al., 1996; Kivelson et al., 1996; 1998). The intensity of Ganymede magnetic field, up to ~1,500 nT in the polar regions (Williams et al., 1997), is sufficiently strong to stand off the Jovian plasma flow, as revealed by the measurements of the Energetic Particle Detector (EPD) onboard the Galileo mission (Williams et al., 1992), in the vicinity of the moon and within its magnetosphere (e.g., Paranicas et al., 1999; Williams, 2001). A non-negligible flux of charged particle populations (mainly Hydrogen, Oxygen and Sulfur ions) impacting the moon's icy surface is believed to activate different release processes, such as sputtering and radiolysis (Marconi, 2007; Plainaki et al., 2015; Leblanc et al., 2017). Modeling of the ion circulation around Ganymede has shown that the bulk population of Jupiter's plasma sheet enters

53 the moon's magnetosphere mainly through the cusps and at low latitudes in the plasma wake
54 hemisphere, most likely through tail reconnection (Poppe et al., 2018). The energetic ions in the keV-
55 MeV range are expected to impact the moon also at regions outside the cusps (see, for instance,
56 Plainaki et al., 2015), inducing ice dissociation and direct sputtering of surface molecules (Bahr et
57 al., 2001; Moore et al., 2007; Teolis et al., 2006, 2017). Laboratory studies revealed that a series of
58 complex surface chemistry processes initiated after ice bombardment by energetic ions, results in the
59 release of H, H_2, O, O_2, OH, and H_2O particles (Johnson, 1990). The characteristics of the energetic
60 particles in the vicinity of the Galilean moons and the release of particles from their icy surfaces have
61 been discussed in the fundamental paper by Cooper et al. (2001). At Ganymede, the ion-induced
62 particle release, together with water sublimation, are believed to generate a tenuous atmospheric
63 envelope around the moon, often referred to as an "exosphere" (e.g., Plainaki et al., 2015). The
64 measurements by the Plasma Science (PLS; Frank et al., 1997b) and Plasma Wave Science (PWS;
65 Eviatar et al., 2001) instruments onboard Galileo, revealed that Ganymede also possesses an
66 ionosphere (Carnielli et al., 2019), consistently with the findings of the Galileo radio occultation
67 experiment (Kliore, 1998).
68
69 Globally, the exosphere of Ganymede consists mainly of sputtered H_2O as well as O_2 and H_2 produced
70 through radiolysis (Johnson, 1990); some other minor species are also expected to be released from
71 the surface through sputtering. The global exospheric environment, therefore, is expected to be
72 formed through a complex process driven by the energy and spatial distributions of the Jovian ion
73 populations, depending at the same time on the moon surface characteristics (e.g. temperature,
74 composition) and the particle release properties (yield, initial energy distribution). Ganymede's
75 neutral environment is believed to be mainly collisionless apart a limited region around the subsolar
76 point where collisions may be present (Marconi, 2007). The exosphere of Ganymede is the actual
77 interface between the icy surface of this moon and Jupiter's magnetosphere. Therefore, its
78 characterization is of key importance to achieve a full understanding of the ice alteration processes

induced by the radiation environment, similarly to the case of Europa (see, for instance, Plainaki et al., 2018 and references therein). For example, the deposition of neutral species from the exosphere onto the moon's surface (e.g., deposition of water) will spectrally mask the weathering products or directly start new chemical patterns. Moreover, the efficiency of both surface weathering and particle release from the surface may be reduced by the ionosphere, which is formed by the ionization of the neutral exosphere. In this view, a number of numerical models have been developed to understand the plasma circulation around this moon as well as the generation of its surface-bounded H_2O exosphere (e.g., Marconi 2007; Turc et al., 2014; Plainaki et al., 2015; Shematovich 2016; Leblanc et al., 2017) and ionosphere (Carnielli et al., 2019). Some evidence for the existence of an exosphere around Ganymede was already provided by the Galileo/UVS (Barth et al.,1996), the HST/GHRS (Hall et al.,1998) and HST/STIS (Feldman et al.,2000) instruments. Recently, the Heterodyne Instrument for the Far Infrared (HIFI) on board the Herschel Space Observatory (Hartogh et al., 2013) observed the vapor H_2O environment of Ganymede. These authors found a difference between the H_2O densities observed at the leading and trailing hemispheres of a factor of 10 and they attributed it to surface composition characteristics, although the uncertainty in their measurements is not negligible.

Several scientific instruments that will operate on board ESA's upcoming Jupiter Icy Moons Explorer (JUICE) mission, have the potential to study Ganymede's H_2O exosphere (Grasset et al., 2013; JUICE definition study report[1]). Among them, the Moons And Jupiter Imaging Spectrometer (MAJIS) will investigate the composition and spatial distribution of water and non-water-ice components in both Ganymede's surface and exospheric environment. There is a strong scientific motivation for speculating on the potential of observing Ganymede's H_2O exosphere during ESA's upcoming JUICE mission. In particular, revealing the characteristics of the near-surface H_2O environment along

[1] http://sci.esa.int/juice/54993-juice-definition-study-report-red-book/

Ganymede's orbit around Jupiter will allow the identification of its source regions and also the efficiency of the particle release from ice, providing at the same time constraints for estimating the energy exchange between the Jovian system and the moon itself. This is due to the fact that the spatial density and energy distributions of Ganymede's H_2O environment reflect the origins of the exosphere generation and the properties of the interaction of the icy surface with the moon's surrounding radiation environment. Indeed, the morphology of the sputtered-H_2O exosphere depends on the topology of the open/closed magnetic field line region, the incident Jovian ion flux and the content of ice contaminants on the surface. In particular, the H_2O molecules released from the surface after its bombardment by Jupiter's plasma and energetic ions follow ballistic trajectories until they return to the surface or they escape or they are lost through ionization or dissociation processes. Upon return to the surface, the H_2O molecules stick there and do not migrate to nearby locations hence remaining confined to their ejection region. This is an important distinction between the H_2O and the O_2 exospheric components. In fact, the O_2 molecules, upon return to the surface, they get thermalized (average kinetic energy $\sim k_bT$) and bounce back to continue their ballistic travel. The process of thermal desorption after the re-impacting of the molecules to the surface is repeated many times until O_2 is either dissociated or ionized. Consequently, contrary to the sputtered-H_2O case, the spatial distribution of the O_2 exospheric density is not directly coupled to its production map upon the surface. Since the H_2O molecules lifetime (before loss) is much longer than the average ballistic flight time, and due to the water's sticking to the ice capability, the spatial distribution of the H_2O exosphere maintains the memory of its origins, providing information on the spatial characteristics of the ice – ion interaction as well as on the sputtering efficiency.

There are further scientific motivations for speculating on the potential of observing Ganymede's H_2O exosphere with JUICE. In particular, the observation of spectral emissions through limb scanning near Ganymede's poles, may provide information related to the preferential access of charged particles to the moon's polar caps furnishing important constraints for the surface weathering

history. The details of the ion access to Ganymede's surface, although attributed to the moon's magnetic field topology, have been long debated in the scientific community. Smith et al. (1979), based on Voyager observations, and Khurana et al. (2007), based on Galileo imaging (see figure 3 of their paper), explained the presence of observed bright polar caps on Ganymede with sputter-induced redistribution and subsequent cold trapping of water molecules, which result in a newer surface, continuously eroded. In particular, Khurana et al. (2007) pointed out a close correspondence between the open-closed magnetic field lines boundary and the boundary of the Ganymede's polar cap that they interpreted as evidence that the latter is associated with charged particle effects. Khurana et al. (2007) suggested also that the equatorial leading/trailing asymmetry (i.e., the albedo of the leading hemisphere is higher than the trailing one; Clark et al., 1986) was due to the preferential flux of ions onto Ganymede's leading hemisphere due to magnetotail reconnection, an hypothesis that was later confirmed by ion-trajectory simulations by Plainaki et al. (2015) and Fatemi et al. (2016). Numerical simulations of both energetic ion precipitation on Ganymede's surface and sputter-induced exosphere generation (e.g. Jia et al., 2009; Plainaki et al., 2015; Poppe et al., 2018) seem to support such a scenario, with respect to both aforementioned points. In particular, simulations by Plainaki et al. (2015) and Poppe et al. (2018) show a shielded region close to Ganymede (at distances < 1.5 R_G) asymmetrically displaced towards the sub-Jovian trailing hemisphere, with enhancements of lower-energy ion flux along the trailing-side boundaries of Ganymede's Alfvén wings. Moreover, enhancements in the flux on the anti-Jovian leading hemisphere are present (Poppe et al., 2018). It's worth noting, however, that current models depend significantly on a series of physical parameter assumptions which are currently poorly known, mainly due to the absence of an adequate quantity of in situ data and also because their quality in terms of spatial and spectral resolution hinder the inference of the necessary properties. Moreover, Ganymede has been mostly observed by ground-based telescopes so far and for this reason the spatial resolution and coverage of the currently available databases are rather limited. For example, the consideration in the models of the moon's magnetosphere morphology (see, for instance, the different approaches by Paty et al. 2008, Jia et al.

155 2009 and Fatemi et al. 2016), or the detailed composition of the icy surface (including impurities) has
156 direct impacts in the modeled sputtering and sublimation rates of the surface. For this reason, and
157 despite the numerous kinetic models proposed in literature, we do not have yet the necessary
158 information to disentangle the influence of different mechanisms on the spectral properties of
159 Ganymede's surface.
160
161 The spectral properties of the exosphere of Ganymede must be resolved for determining the properties
162 of the space environment of Ganymede and for accurately mapping ion precipitation to the icy
163 surface, a key mechanism linking the moon itself to the Jovian magnetospheric environment. In this
164 paper, we investigate the possibility for MAJIS to observe spectral emission signatures of
165 Ganymede's H_2O exosphere, such as the non-Local Thermal Equilibrium (non-LTE) photon
166 emissions from water molecules, using different modelled density profiles. First, we compare the
167 existing models of Ganymede's water exosphere. We then use these model outputs to estimate the
168 different scenarios for the expected IR emission from water molecules. In particular, in Section 2 we
169 briefly review the generation mechanisms of Ganymede's H_2O exosphere and discuss how the
170 morphology of the neutral environment depends on the properties of the charged particle circulation
171 around the planet. We also discuss the environment characteristics derived by different models. In
172 Section 3 we present the main characteristics of the MAJIS instrument relevant for our investigation
173 and we estimate the expected signal non-LTE photon emission from the water exospheric molecules.
174 Endogenic processes can also contribute to exospheric density enhancements. In particular, ongoing
175 cryovolcanic activity has been identified on Enceladus, and probably on Europa, through the
176 observation of water (gas and ice) plumes (Porco et al., 2006; Sparks et al., 2017). Although no such
177 evidence has been found so far for Ganymede, the JUICE mission offers a unique opportunity for
178 searching for such an activity in geometric configurations not accessible from the Earth's orbit. In
179 this regard, remote observations in visible and near-infrared spectral range at very high solar phase
180 angle (or even in solar occultation geometry, if possible) are the most promising, since a plume

scatters solar light much more efficiently in the forward direction. In Section 4, we try to establish the potential observability of these phenomena with MAJIS, considering different observing study cases representative of different mission phases. In Section 5, we discuss the results of our calculations and present a summary of conclusions together with some future plans to optimize MAJIS observations.

2. Generation of the water vapor exosphere of Ganymede

The role of Ganymede's mini magnetosphere

The plasma-surface interactions guided by Ganymede's intrinsic magnetic field are the main drivers of the H_2O exosphere generation. The major plasma source in Jupiter's magnetosphere is the volcanic-active moon Io which ejects material that becomes dissociated and/or ionized by the solar EUV radiation (Broadfoot et al., 1979), generating predominantly multiply charged Oxygen and Sulfur ions (Bagenal et al. 1996). At Ganymede's distance from Jupiter, the plasma is confined to a low scale height current sheet (also called Jupiter's Plasma Sheet - JPS) cantered roughly around the Jovian magnetic equator (Khurana et al., 2004; 2007). Because of the 10^0 tilt of Jupiter's magnetic field to the planet's rotational axis, the current sheet oscillates up and down Ganymede's orbital plane. Within the plasma sheet and up to a distance of ~ 10 R_J from Jupiter, the plasma slightly subcorotates at v ~ 150 km/s, whereas at the distance of Ganymede (at about 15.3 R_J from Jupiter) it lags the corotation, in the azimuthal direction, by 37 km/s (Kivelson et al., 2004). At Ganymede, the Jovian magnetospheric plasma is characterized by a thermal component with density, n_e, ~5–20 cm^{-3}, and temperature, T_e, ~ 20 eV plus a suprathermal component with n_e~0.5–2cm^{-3}, T_e ~ 2keV (Scudder et al., 1981). The bombardment of Ganymede's surface by high energy ions induces radiolysis and direct sputtering of surface molecules that populate the moon's exosphere (Cassidy et al., 2013). The generation and evolution of the exosphere of an icy moon is a complex process that depends on the environment properties (e.g. spectrum and flux spatial distribution of Jupiter's magnetospheric ion

population), the characteristics of the moon's surface (e.g. composition, impurities, temperature), as well as the moon's orbital phase around Jupiter (see, for instance, Plainaki et al., 2013; Leblanc et al., 2017). There is a widespread consensus that Jupiter's energetic ion environment provides the major contribution to the generation of Ganymede's exosphere although some alternative scenarios, such as secondary sputtering by ionospheric ions or water sublimation, cannot be excluded. Locally, in regions near the subsolar point, where the maximum diurnal temperatures are reached (up to 152 K; Orton et al., 1996) sublimated water is believed to be the dominant exosphere component. Several modelling efforts have advanced our understanding of the generation of Ganymede's exosphere providing important constraints for the involved processes. As in the Europa case, exospheric models are based on very different approaches employing a variety of parameters and assumptions that result in a large range of values for the obtained outputs. For a general description and comparison of the available techniques for studying the exospheres of the Galilean satellites see the works by Marconi (2007), Shematovich (2016), Plainaki et al. (2018) and references therein.

Since the role of the moon's bombardment by energetic ions is crucial for the generation of the sputter-induced H_2O exosphere, significant effort has been devoted to simulating the ion circulation around Ganymede and precipitation to the surface. Some of the models do provide maps of the precipitation of plasma and charged energetic particles to the moon's surface as well as estimates of sputtering rates. For instance, Paranicas et al. (1999) assumed that sputtering takes place in the polar caps, which they defined as the surface area above the latitude of $\pm 45^0$, and they estimated a total rate of $2 \cdot 10^{26}$ s^{-1}. The electric and magnetic fields determining the charged particle trajectories differ among different magnetospheric models considered in literature (see, for example, Jia et al. 2009, Fatemi et al. 2016, and references therein). Cooper et al. (2001) performed a back tracing technique to simulate ion circulation within Ganymede's magnetosphere with only superimposed magnetic fields based on Galileo data from the G2 flyby; the total sputtering rate estimated by these authors was $\sim 4.3 \cdot 10^{26}$ s^{-1}.

Plainaki et al. (2015) used the electric and magnetic fields from the Jia et al. (2009) global Magnetohydrodynamic (MHD) model of Ganymede's magnetosphere to trace energetic charged particle trajectories around the moon and to identify the regions where ions hit the ice activating particle release through sputtering and radiolysis. In particular, three singly charged energetic species (H^+, O^+, and S^+) at a selection of discrete energies ranging between 1 and 100 keV, were considered. To absolutely normalize the flux of incident energetic particles, they used the distributions for each species as determined by Paranicas et al. (1999). For each specific pair of ion composition and energy, 10^8 particles were simulated to ensure sufficient statistics. The total O^+ precipitating flux integrated in energy in the simulation by Plainaki et al. (2015) is shown in Figure 1. The total H_2O sputtering rate estimated by Plainaki et al. (2015) was $7 \cdot 10^{25}$ s^{-1}. Recently, Poppe et al. (2018) developed a backwards ion tracing model to define the energetic ion population characteristics in the near-Ganymede space. They used the three-dimensional, self-consistent hybrid model simulations of Ganymede's magnetospheric interaction with the Jovian magnetosphere by Fatemi et al. (2016) to obtain the electric and magnetic field needed for their single-particle simulations. In the simulations by Poppe et al. (2018) three energetic species, H^+, O^{++}, and S^{+++}, at three discrete energies, 30 keV, 300 keV, and 3 MeV were considered. We note that the MHD model by Jia et al. (2009) is single-fluid (O^+) whereas Fatemi et al. (2016) have implemented a hybrid plasma model (kinetic ions and fluid electrons) using only the thermal component (i.e., non energetic particles). Although the simulations by Plainaki et al. and Poppe et al. did not consider exactly the same inputs (e.g. ion energy spectrum; magnetic field model), the results of their simulations are generally in good agreement. Both studies show that there is a decrease in the ion flux from the upstream boundary at a distance of ~ 2 R_G approaching the moon. Moreover, there is a shielding from the ions region on the surface within the distance of ~ 2 R_G from Ganymede's center, where R_G is Ganymede's radius. The exact dimension of this shielded region depends on the magnetic rigidity of the ions considered (higher rigidity ions have access on the surface at lower latitudes). Enhancements in the energetic ion flux downstream of Ganymede were also found by both models. Both the simulations by Plainaki et al.

(2015) and Poppe et al. (2018) showed enhancements extending vertically along the upstream boundaries of the Alfvén wings, however the morphologies of the flux distribution are not identical; indeed, the magnetic field model considered in each case determines the details of the deceleration process of the incident ion flux upon entering the Alfvén wings and the deflection of incident trajectories from the near-equatorial plane to the polar regions. Over Ganymede's polar caps the flux is diminished whereas downstream both simulations show evidence of trapped populations and a reconnection region within Ganymede's magnetotail at distances between 2 and 4 R_G.

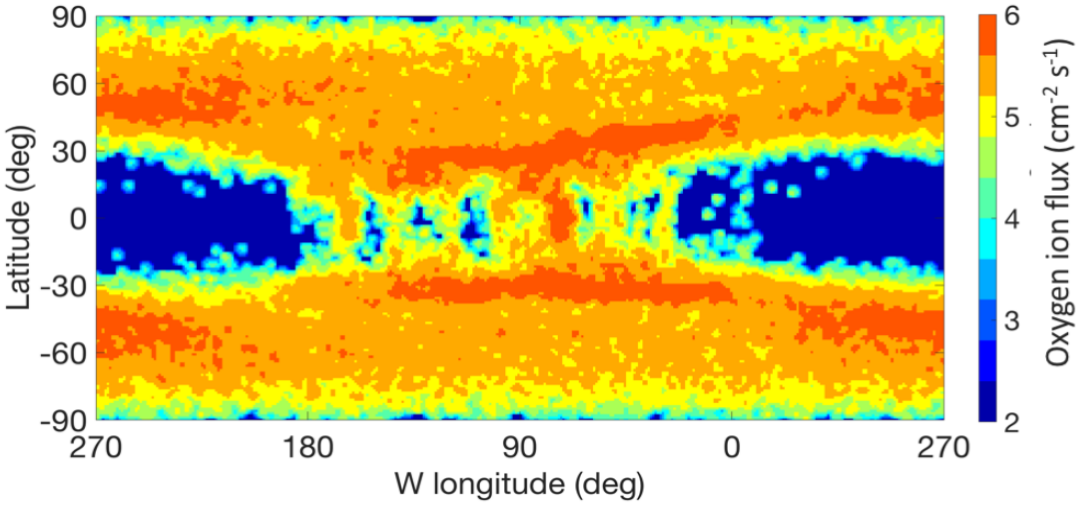

Figure 1: Integral O^+ flux (in cm^{-2} s^{-1}) precipitating at Ganymede's surface based on simulations by Plainaki et al. (2015) considering an ion energy range from 1 keV to 100 keV. In the coordinate system used in this plot, the leading hemisphere apex is at longitude 90^0 and the sub-Jovian point at longitude 0^0. The MHD model used for the simulations considers conditions similar to those during the Galileo G8 flyby (Ganymede was near the center of Jupiter's plasma sheet).

Exosphere models

Moon exospheres have been discussed many times in the past, also through a comparative planetology approach (see, for example, the collection of papers published by Coustenis et al. (2010)). Our knowledge on the configuration of Ganymede's H_2O vapor exosphere is currently largely based on modelling efforts. Exospheric models are in general based on very different approaches (e.g., the

assumption of a collisional or a collisionless environment) and usually include H_2O and other exospheric species as well.

The 2-D axisymmetric Direct Simulation Monte Carlo (DSMC) model by Marconi (2007) used a multispecies approach to derive the atmospheric O_2, H_2O, H_2, and H, O, and OH spatial structure, considering the non-uniform distribution of the surface temperature based on the PLS measurements by Galileo. Marconi (2007) found that near the subsolar point the dominant component is H_2O vapor, whereas near the polar regions the main component, at low altitudes, is molecular Oxygen; the uppermost layers of the exosphere are populated by molecular hydrogen according to this model. A similar approach was also followed by Shematovich (2016) who showed that collisions are responsible for the observed H_2O and O_2 concentration at altitudes between 10 and 100 km from the surface.

Ganymede's exosphere has been studied also through 3-D test-particle models (e.g. Turc et al., 2014; Plainaki et al., 2015). Turc et al. (2014) assumed a collisionless 3-D model approach for simulating Ganymede's exosphere above the sunlit trailing hemisphere. The Lyman-α emission brightness obtained based on the model by Turc et al. (2014) was found much smaller than the one observed by Barth et al. (1996). The modelled exosphere is clearly structured by the two particle surface sources, sputtering and sublimation, resulting in a strong dichotomy between the subsolar region, where sublimation takes place, and the rest of the exosphere. Far away from the subsolar region, O_2 is accumulated close to the surface; instead, the lighter H_2 is found at higher altitudes, even above the subsolar region.

The model by Plainaki et al. (2015) was the first one to take into account the effect in the exosphere generation of the ion precipitation to the moon's icy surface. This 3-D single-particle Monte Carlo model was based on the previously released Europa Global model of Outgoing exospheric neutrals

304 (EGEON, Plainaki et al. 2010;2012; 2013) as well as previous efforts for simulating Mercury's
305 exosphere (Mura et al., 2009). Plainaki et al. (2015) assumed that the main sources of Ganymede's
306 neutral environment are ion sputtering, radiolysis and water ice sublimation. The EGEON code takes
307 into account the exact angle of incidence for the ions impacting the surface. It was shown that the
308 morphology of the exosphere is significantly determined by the aforementioned processes and,
309 moreover, for the sputtered-H_2O case, there is a large difference in the concentrations of neutral
310 components between the high and low latitude regions of the exosphere. Figure 2 shows the density
311 spatial distribution of Ganymede's sputtered-H_2O exosphere according to the EGEON model.
312 Moreover, Plainaki et al. (2015) considered H_2O-sputtering yields depending on the incident ion
313 energies and therefore their exospheric model, contrary to previous ones, was based on a sputtering
314 efficiency that was spatially variable. Loss processes have also an important role in the exosphere
315 spatial distribution. Plainaki et al. (2015) incorporated in their model different plasma-induced loss
316 processes (see their table 4) among which charge exchange between low-energy charged particles
317 and exospheric molecules. Atmospheric sputtering can be an important sink for planetary and lunar
318 neutral environments, as discussed in detail by Johnson (1994), depending on the relative bulk motion
319 between plasma and neutral particles (see also discussion in Plainaki et al. (2015) and references
320 therein). In EGEON, the estimated loss rate of Ganymede's H_2O exosphere due to charge exchange
321 is of the order of $\sim 10^{-5}$ s^{-1}. The importance of this process was highlighted also for the Europa case
322 in the studies by Saur et al. (1998), Dols et al. (2016) and Lucchetti et al. (2016). Plainaki et al. (2015)
323 showed that the spatial distribution of the sputtered H_2O molecules reflects the characteristics of the
324 interaction between Ganymede and Jupiter's magnetospheric particles. In particular, in the full-
325 mirroring approximation for the ion precipitation pattern, it was shown that the H_2O exosphere is
326 efficiently sputtered both in the polar region and the low latitude wake hemisphere. We note here that
327 both studies by Marconi (2007) and Plainaki et al. (2015) argue that the neutral environment is largely
328 collisionless, except for a small region near the subsolar point.
329

330 Recently, Leblanc et al. (2017) studied Ganymede's neutral environment taking into account Jupiter's
331 gravitational influence and the evolution of the exosphere along the moon's orbit around the giant
332 planet. Their 3-D Monte Carlo model considered water sublimation and sputtering as the main
333 exosphere sources, and electron impact ionization and dissociation as well as particle-surface
334 interactions, as loss processes. The model follows the dynamical evolution of the exosphere as
335 Ganymede orbits Jupiter. The neutral species considered in this model were O_2, O, H_2O, H, H_2, and
336 OH released after the surface bombardment by incident Jovian ions. The model by Leblanc et al.
337 (2017) assumed that Jovian ions precipitate to the surface within the open field line regions. In
338 particular, the model considered the open-closed magnetic field lines boundary (OCFB) as derived
339 by the auroral observations described in McGrath et al. (2013). According to these authors, the
340 Ganymede exosphere appears to be highly stratified in density and composition due to the variation
341 of the ejection mechanisms and motion of the ejected molecules over the moon's orbital period. The
342 fate of the ejecta is also species-dependent due to the species dependent surface interactions. Leblanc
343 et al. (2017) confirmed the difficulty in providing a precise estimation of the water sublimation being
344 this process very sensitive in temperature variations and surface composition properties. Last, they
345 argued that the consideration of collisions among the particles in Ganymede's exosphere has a minor
346 effect in the density distribution. In Table 1 we summarize the assumptions and main findings of
347 current models of Ganymede's H_2O exosphere.
348

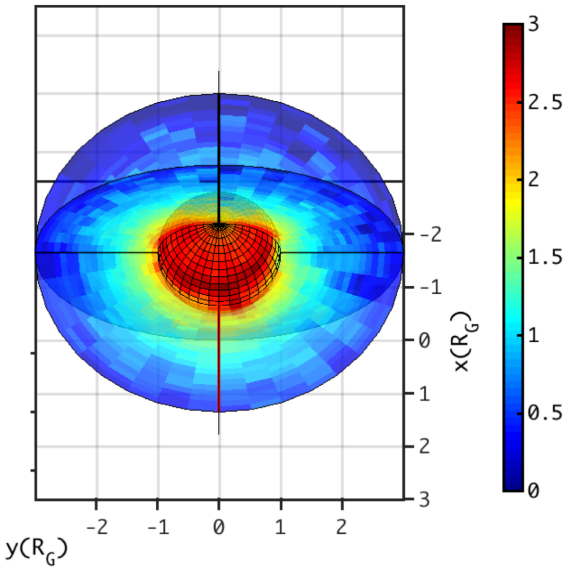

Figure 2: Density spatial distribution of Ganymede's sputtered-H_2O exosphere according to the model by Plainaki et al. (2015), as seen from the north, at a viewing angle between 0 ^{o} and 90^o with respect to the equator. The scale is logarithmic and density is measured in particles/cm^3. To calculate the ion surface precipitation pattern, a necessary input for EGEON, the full-mirroring approximation has been considered (for details see Plainaki et al. 2015). H_2O is efficiently sputtered in the polar regions as well as in the low latitude wake hemisphere (leading hemisphere). In the coordinate system used in this plot, the orbital direction is along the positive x axis whereas Jupiter is towards the positive y axis.

Table 1: Ganymede's H_2O exosphere: comparison of model assumptions and main findings

H_2O-exosphere model	**Ion –surface interaction morphology**	**Technical characteristics Notes**	**H_2O release rate at the surface**	**Exosphere scale-height**
Marconi (2007)	N/A	DSMC model	sputtering: 1.5×10^{26} s^{-1} sublimation: 7×10^{29} s^{-1}	70 km

Shematovich (2016)	N/A	DSMC model	sputtering: 1.6×10^{26} s^{-1} (Cooper et al. 2001) sublimation: as in Marconi (2007)	80 km
Turc et al. (2014)	guided by field lines that are assumed to be closed at latitudes below ±45° and open above the polar regions	collisionelss single-particle Monte Carlo model	sputtering: 1.5×10^{26} s^{-1} sublimation: as in Marconi (2007)	65 km
Plainaki et al. (2015)	guided by the MHD-model by Jia et al. (2009); ion circulation simulations have been performed	collisionless single-particle Monte Carlo model ion circulation simulations are used as an input for the estimation of the exosphere	sputtering: 7×10^{25} s^{-1} (estimated within the model assuming the Famà et al. (2009) yields and ion spectrum by Paranicas et al. (1999)) sublimation: as in Marconi (2007)	55 km
Leblanc et al. (2017)	taking place at the regions of the open field lines as defined by the McGrath	collisional Monte Carlo model consideration of the dynamical evolution	sputtering: 8×10^{27} s^{-1} sublimation: 8×10^{21} s^{-1} (low sublimation scenario)	~ 400 km

	et al. (2013) auroral observations	of the exosphere along the moon's orbit		

Figure 3 presents a comparison between the H_2O density profiles calculated by different models. We note that around the subsolar point and up to an altitude of at least ~250 km, all models have the same trend, with the exception of the model by Leblanc et al. (2017), where low sublimation rate is considered ab initio. We note that the consideration by Leblanc et al. of a low sublimation rate was motivated by the matching of the observed ratio of the H_2O column density between the leading and trailing hemispheres (Hartogh et al., 2013). All models agree that the environment is collisional only locally, i.e. near the subsolar point, assuming that the underlying surface region is mainly composed from ice. The Marconi (2007), Plainaki et al. (2015) and Turc et al. (2014) models agree that the maximum H_2O density above the subsolar surface region is of the order of 10^9 cm^{-3}, whereas for the model by Shematovich (2016) the peak density is ~ 10^8 cm^{-3}. Models begin to diverge substantially at higher altitudes (above ~200 km). In that region, the density of the sublimated exosphere is significantly decreased, as shown in the collisionless model by Plainaki et al. (2015) hence any diversion of a model from a strictly thermal profile is likely the result of either the assumed chemistry taking place within the exosphere or of the assumed initial energy distribution upon the particle release from the surface.

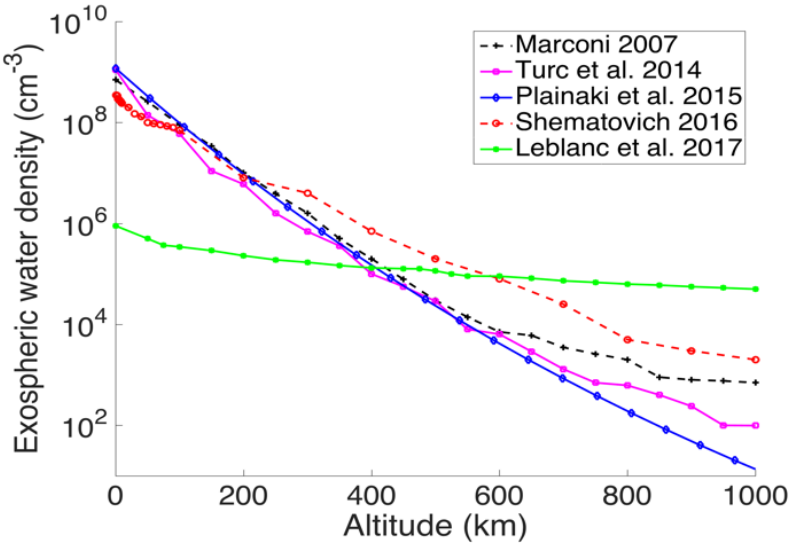

Figure 3: H_2O density profiles of Ganymede's exosphere above the subsolar point, as estimated by different models.

3. Detecting Ganymede's water vapor exosphere with JUICE/MAJIS

The ESA JUICE mission (Grasset et al., 2013), whose launch is scheduled in 2022, will explore the icy Galilean satellites thanks to a series of flybys of Callisto, Ganymede and Europa, prior to finally entering orbit around Ganymede, the mission's main target. The Ganymede dedicated orbit is divided into a high altitude (~5000 km) circular orbit phase (GCO-5000), including two elliptical orbit sub-phases, expected to last about 120 days, and a medium altitude (~500 km) circular orbit (GCO-500) phase, at least 150 days long. During periods in between flybys, observation time will be devoted also to the study of Jupiter's atmosphere, magnetosphere and auroras. The investigation of Ganymede's exosphere through the analysis of hyperspectral VIS-IR data is among the science objectives of MAJIS. In particular, MAJIS will investigate the non-LTE exospheric emissions by observing the satellite' limb at different locations and geometries, so as to assess the abundance of the exospheric component. A brief example of possible science investigations with JUICE related to

393 the icy satellite exospheres has been recently proposed by Plainaki et al. (2018; see paper's Section
394 4).
395
396 The MAJIS experiment onboard JUICE is led by a French-Italian consortium (Langevin et al., 2018;
397 Piccioni et al., 2014). MAJIS is a compact visible and near-infrared imaging spectrometer covering
398 the spectral range from 0.5 to 5.54 μm, split in two channels (Piccioni et al., 2019; Guerri et al., 2018).
399 The VIS-NIR spectral channel covers the 0.5-2.35 μm band with an average sampling of 3.66
400 nm/band. The IR channel works in the 2.25-5.54 μm range with a 6.51 nm/band average sampling.
401 The optical design of the MAJIS instrument relies on a f/3.2 aperture Three Mirrors Anastigmatic
402 (TMA) telescope (pupil equivalent diameter is 75 mm; focal length is 240 mm), matching two camera
403 imaging spectrometers, sharing the same entrance slit by means of a collimator. A dichroic element
404 is used to split the light beam between the two spectral channels (VIS-NIR and IR). The operative
405 temperature of the Optical Head (<140 K) and the cryogenic IR detector temperature (<90 K) are
406 achieved through passive cooling. Two detectors with similar format are foreseen for both
407 spectrometers comprising an array of 800 x 1016 pixels. Binning by 2 will always be applied in the
408 spatial direction (400 pixels). Binning by 2 is also nominal in the spectral direction (508 spectral
409 elements), leading to a 36 μm pitch, but up to 264 spectral bands can be acquired without spectral
410 binning, leading to a frame 400 pixels x 640 spectral element. The resulting Instantaneous Field of
411 View (IFOV) is 150 μrad, while the MAJIS FOV along the slit is ±1.7°. The IFOV size corresponds
412 to resolutions of 75 m/px and 300 m/px when observing respectively at nadir and at limb from a 500
413 km circular orbit around Ganymede. The instrument has a high operational flexibility thanks to a
414 series of technical capabilities. A steerable mirror in the telescope allows MAJIS to acquire
415 bidimensional hyperspectral images through consecutive scans and to compensate for the spacecraft
416 motion during the GCO-500 orbital phase or during flybys. A series of different operational modes
417 have been pre-set allowing spatial and spectral binning. Radiation noise due to charged particle
418 populations can be reduced through a despiking algorithm based on sub-frame sorting and summing,

419 also useful to increase the on-board data compression rate for effectively reducing the data downlink
420 volume (Langevin, 2018). Spatial and spectral binning beyond the nominal level (36 μm pitch) will
421 be implemented in order to optimize the data volume when providing extensive spatial coverage of
422 the icy satellites at medium resolution (1 to 5 km/pixel) as well as time evolution sequences for the
423 atmosphere of Jupiter and the exospheres of satellites. In Table 2, the most significant
424 characteristics of MAJIS are summarized, while more details can be found in Guerri et al. (2018) and
425 Piccioni et al. (2019).
426
427 Apart from the search for possible plumes (which will be discussed in the next section), the MAJIS
428 limb measurements are relevant to the search for H_2O exospheric emission. The most favorable
429 observing condition in this case is when the Line Of Sight (LOS) within the exosphere is totally
430 illuminated. In this case, due to effective radiative pumping, a non-LTE photon emission signal from
431 water vapor will be occurring and can in principle be strong enough to be revealed by MAJIS. In
432 particular, the MAJIS spectral range covers the H_2O non-LTE emission bands between 2.4 and 3 μm.
433 The ν_3 H_2O band at 2.67 μm is the strongest one in this spectral range and we expect to observe it
434 together with the ν_1 and ν_2 H_2O bands. Since Ganymede's exosphere is as optically thin as the
435 cometary atmospheres, we expect fluorescence to be the main excitation mechanism for the H_2O
436 bands (Crovisier, 1987; Bockelée-Morvan, 1987; Bockelée-Morvan et al., 2004). To estimate,
437 therefore, the non-LTE radiance to be measured from a spectrometer on board a spacecraft in limb
438 viewing, we follow the approach suggested by Bockelée-Morvan et al. (2015) and Villanueva et al.
439 (2012). That being the case, we are able to obtain a first simulation of the MAJIS observations of
440 Ganymede's H_2O exosphere. In this exercise, we consider currently available H_2O exosphere models
441 (see previous section) together with the instrument performance parameters. In this paper, we do not
442 perform estimations corresponding to the sublimated water density estimated by Leblanc et al. (2017).
443 The sublimation rate assumed by these authors is significantly lower than the ones considered by the
444 other models resulting in a significantly reduced Signal-to-Noise Ratio (SNR). The assumption of

445 such a low sublimation rate has its origin to the matching of the observed ratio of the H_2O column
446 density at the leading and trailing hemispheres (Hartogh et al., 2013), nevertheless, since the
447 methodology for deriving this quantity and the related uncertainty in the estimation are not yet clear
448 we prefer to take into account only the sublimation rate estimations available in published literature.
449 The estimations presented here are likely to be reviewed in the next years also due to theoretical
450 model updates hence the scope of this paper is to provide an indicative range for the expected
451 exospheric measurements.
452
453
454
455 **Table 2**: Basic technical characteristics of MAJIS. For a detailed description of the instrument the
456 reader is referred to Guerri et al. (2018) and Piccioni et al. (2019).
457

Basic technical characteristics of MAJIS	
Spectral range	0.5 - 5.54 μm *VIS-NIR channel:* 0.5-2.35 μm *IR channel*: 2.25-5.54 μm
Spectral sampling	*VIS-NIR channel* 3.66 nm/band *IR channel*: 6.51 nm/band
FOV along the slit	±1.7°
IFOV	150 μrad
OH operative temperature	110 - 160 K
VIS-NIR detector operative temperature	130 K (nominal)
IR detector operative temperature	90 K (nominal)

458
459

460 To estimate the expected non-LTE radiance we extract the line parameters from the HITRAN
461 database (Gordon et al., 2017) and we compute the cross-sections σ (in cm^2) for the roto-vibrational
462 lines of the ν_1, ν_2 and ν_3 H_2O band. We assume band emission rates (g-factors), gf, equal to 3.349 ×
463 10^{-4} s^{-1}, 3.33×10^{-5} s^{-1} and 2.67×10^{-4} s^{-1} for the H_2O ν_3, ν_1 and ν_2 bands, respectively (Villanueva
464 et al., 2012). Since the aforementioned values refer to at the heliocentric distance of 1 AU, their
465 rescaling to 5.2 AU, is required.
466 The band integrated radiance (in W m^{-2} sr^{-1}) can be estimated as follows:
467
468 $$I_{i,l} = \frac{(h\cdot\underline{\upsilon})}{(4\cdot\pi)} \cdot gf_i \cdot N_l \quad (1)$$
469 where $\underline{\upsilon}$ is the central frequency of the band, h is the Planck constant, N_l (in m^{-2}) is the column density
470 along the LOS inside the l exospheric level. The i index characterizes the H_2O spectroscopic
471 transition. Since the band integrated radiance can be also written as
472 $$I_{i,l} = f_{i,l} \cdot \int \sigma_{i,l}(\upsilon) d\upsilon \quad (2)$$
473 where $f_{i,l}$ is a conversion parameter (in W cm^{-4} cm sr^{-1}), based on Eq.s. (1) and (2), the emitted
474 radiance $R_{i,l}$ (in W m^{-2} cm sr^{-1}) along the LOS inside the l exospheric level and for the i transition can
475 be written as
476 $$R_{i,l}(\upsilon) = f_{i,l} \cdot \sigma_{i,l}(\upsilon) = \frac{h\cdot\upsilon\cdot gf_i\cdot N_l}{4\cdot\pi\cdot\int \sigma_{i,l}(\upsilon)d\upsilon} \cdot 10^4 \quad (3)$$
477 Considering all the spectroscopic transitions and exospheric levels occurring along the LOS, the
478 radiance at the detector is:
479 $$R(\upsilon) = \sum_i \sum_l R_{i,l}(\nu) \quad (4)$$
480 The radiance R computed so far has a very high spectral resolution equal to $2\text{x}10^{-3}$ cm^{-1} chosen as the
481 best compromise between the inclusion of the spectroscopic lines and the required computational
482 time. We then convolve R with the MAJIS IR channel instrumental line shape expected to follow a

Gaussian profile with a conservative Full-Width-Half-Maximum FWHM estimated at 12.98 nm corresponding to a factor of two times the spectral sampling of 6.49 nm (Guerri et al., 2018).

During Ganymede flybys as well as in Ganymede orbits, all exosphere observations are planned with the slit oriented parallel to the limb. This is the best configuration as the whole slit would be exposed to the maximum exosphere signal while reducing possible straylight from the surface, and the sensitivity of the measurement to the tangent altitude would be maximum as well. In Figure 4 we show the geometry of a hypothetical observation taking place at UTC 2032-09-15 T09:42:42, with JUICE being distant ~7700 km from the center of Ganymede (altitude of 5100 km), with a spatial resolution of ~ 0.75 km at the sub-spacecraft point and ~ 1 km in terms of altitude resolution of the exosphere at the limb.

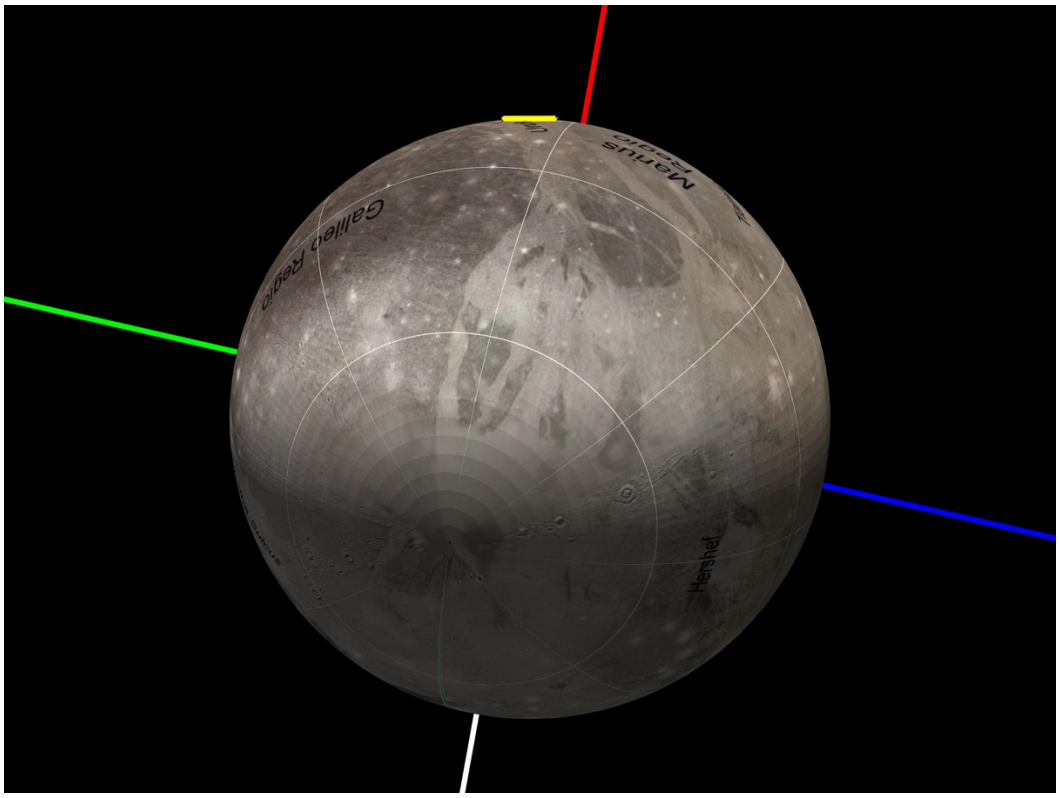

Figure 4: Observation of Ganymede exosphere on 2032-09-15 T09:42:42 in CREMA 3.0 with limb pointing by MAJIS and the MAJIS slit oriented parallel to the limb. MAJIS FoV is the yellow

498 segment. Colored lines indicate directions towards Jupiter (white), anti-Jupiter (red), leading (green)
499 and trailing hemisphere (blue). This attitude is a preliminary estimation: technical constraints such as
500 solar illumination on panels are still to be evaluated.
501
502 Most exospheric observations during Ganymede flybys will be made at relatively large distances
503 (e.g., 40000 km corresponding to a spatial resolution of 6 km/px) as closer observations conflict with
504 remote sensing and geophysics observations of Ganymede. The most favorable phase for Ganymede
505 exospheric observations is the near circular phase of GCO-5000 (120 days-long) and the two adjacent
506 elliptical phases (2 x 15 days) as all latitudes can be observed in the optimum geometry (limb pointing
507 with the MAJIS slit parallel to the limb) on orbital segments extending from the night side up to the
508 pole. In this case pointing can be driven by exospheric observations whereas most remote sensing
509 observations of the surface will be made on the day side of the GCO-5000 orbit. When the spacecraft
510 is at an altitude of ~ 5000 km the spatial resolution when pointing at the limb is 1.07 km/px. The
511 dwell time is ~ 1 s as the orbital velocity is 1.1 km/s. Such integration times lead to relatively low
512 SNR. SNR can be improved by extending the repetition time at the expense of vertical spatial
513 resolution. As the MAJIS slit is tangent to the limb, one can co-add spatial pixels without degrading
514 the vertical spatial resolution at the center of the slit (closest to the limb). Since the co-adding
515 technique involves only adjacent bins along the slit, which is oriented tangent to the limb, the worst
516 binned spatial resolution is ~17 km/px. We note that the considered exospheric model has a horizontal
517 spatial resolution of about 1/10 R_G, which is much higher than the worst spatial resolution we can
518 have along the slit. Therefore, we can assume our exospheric conditions as homogeneous within the
519 co-added bin. Moreover, during the other planned JUICE orbital phases around Ganymede (e.g.,
520 GCO-500), the distance of the spacecraft from the target will be lower than the one we considered
521 here and this will further improve the MAJIS spatial resolution with respect to the fixed horizontal
522 spatial resolution of current exospheric models.
523

The noise level is estimated using the MAJIS radiometric model, taking into account the repetition time and the despiking strategy (sub-integration time and number of selected sub-integrations after sorting). An example of the signal we expect to measure between 2.4 and 3 μm (the spectroscopic range with stronger H_2O line intensities) is shown in Figure 5. These simulations, based on the Plainaki et al. (2015) model extended in altitude up to 1000 km, are performed at a tangent latitude of ~10°N, assuming the LOS within the exosphere totally illuminated. For completeness, we also estimated the SNR corresponding to the exospheric models of Marconi (2007; Figure A1), Shematovich et al. (2016; Figure A2), and Turc et al. (2014; Figure A3) which are presented in the appendix.

Two representative observation cases have been considered for observations from GCO-5000:

- High vertical resolution: 1.1 s repetition time, binning x 4 along the slit (projected IFOV: 1.1 km vertical, 4.3 km along slit); despiking strategy: lowest of 3 CDS with 0.1 s integration time.
- Low vertical resolution: 9 s repetition time, binning x 16 along the slit (projected IFOV: 10 km vertical, 17 km along slit); despiking strategy: average of 3 lowest CDS out of 6 with 0.643 s integration time.

The estimated SNR at peak intensities have been evaluated in Table 3 for both observational modes at latitude ~10°N and three tangent altitudes (10 km, 50 km and 100 km). Such observations will provide constraints on actual H_2O column densities as a function of altitude, making it possible to adjust the observation strategy for exospheres once in Ganymede orbit.

Table 3: Observing the water exosphere of Ganymede with MAJIS. The Signal-to-Noise Ratio (SNR) has been evaluated for high vertical resolution observations (spatial resolution 4.3 km along slit x 1.1 km vertical) and low vertical resolution (17 km along slit x 10 km vertical) as a function of the tangent altitude for different H_2O exospheric models.

Model	Tangent altitude (km)	MAJIS SNR (high vertical res.)	MAJIS SNR (low vertical res.)
Marconi (2007)	10	12.6	178
Marconi (2007)	50	5.62	79.2
Marconi (2007)	100	1.98	27.8
Plainaki et al. (2015)	10	16.6	234
Plainaki et al. (2015)	50	4.07	57.2
Plainaki et al. (2015)	100	1.03	14.4
Shematovich (2016)	10	4.82	67.9
Shematovich (2016)	50	2.73	38.5
Shematovich (2016)	100	1.94	27.3
Turc et al. (2014)	10	16.0	225.8
Turc et al. (2014)	50	3.08	43.3
Turc et al. (2014)	100	1.22	17.1

Figure 6 shows the estimated SNR as a function of wavelength for high vertical resolution with different exosphere models. Our simulations using the models by Marconi (2007), Plainaki et al. (2015), Shematovich (2016), and Turc et al. (2014), indicate that MAJIS provides outstanding capabilities for observing water in Ganymede's exosphere in limb observations at tangent altitudes below 100 km from the surface and at latitudes ± 10°. The upcoming measurements with JUICE of Ganymede's exosphere are therefore expected to represent a significant test for the currently available exospheric models providing at the same time important feedback for developing more comprehensive scenarios.

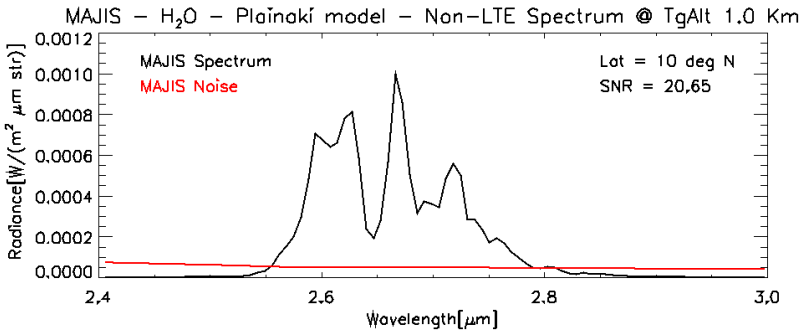

557

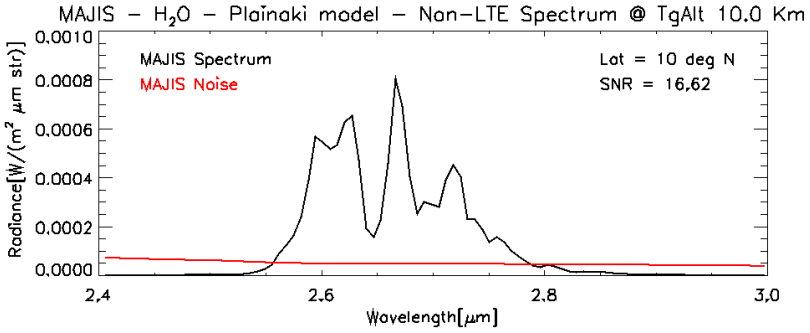

558

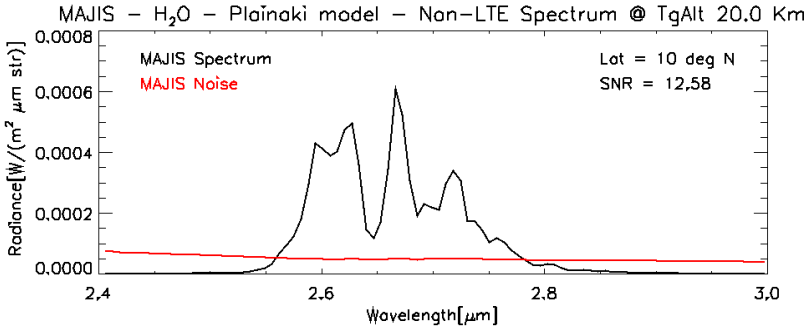

559

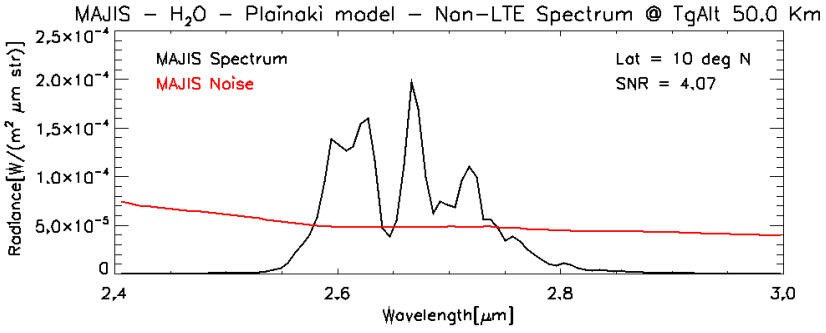

560

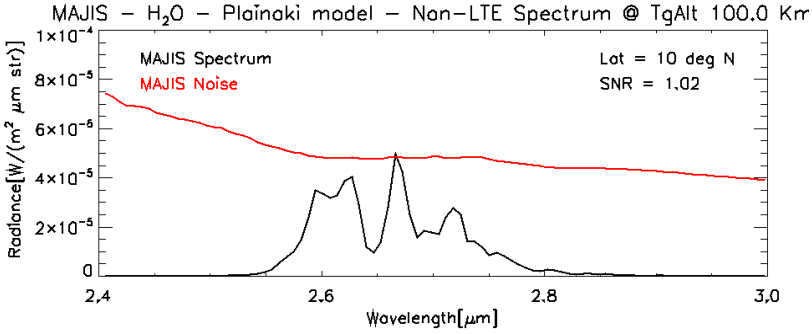

561

Figure 5: Simulated MAJIS spectrum (black line, IR channel, nominal detector temperature = 90 K) of the H_2O Non-LTE emission between 2.4 and 3 microns for the Ganymede exosphere model by Plainaki et al. (2015) at lat~10°N and tangent altitudes of 1, 10, 20, 50, and 100 km. Red line indicates the predicted Noise Equivalent Spectral Radiance (NESR) of the MAJIS instrument for high vertical resolution observations.

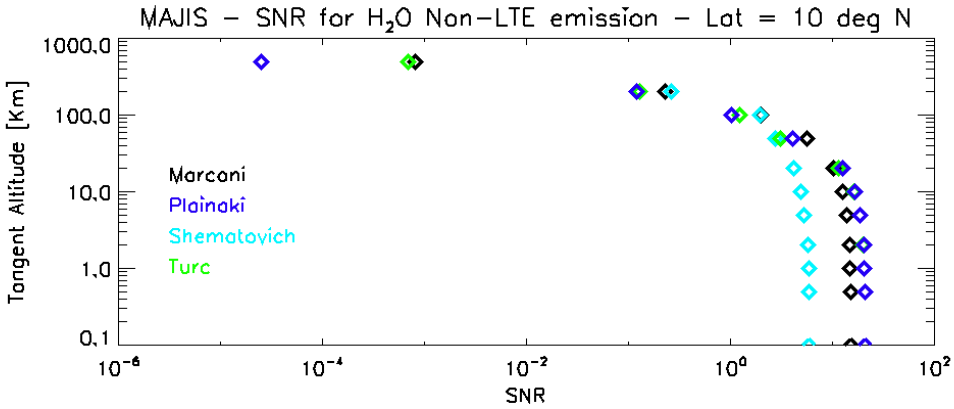

Figure 6: Comparison of the MAJIS signal-to-noise ratios for H_2O non-LTE emission for high vertical resolution observations computed for different exospheric models as a function of observation tangent altitude at latitude ~10°N. See text for details.

Several parameters related to the water deposition on the surface (e.g., the spatial distribution of the H_2O abundance on Ganymede's surface, the albedo map) are expected to be linked to the impact of the external environment. Recently, studies based on VLT/SINFONI data (1.40–2.50 μm) showed that the abundance maps of H_2O-ice on Ganymede's surface are characterized by a latitudinal gradient linked to the magnetosphere ion bombardment (Ligier et al. 2019). Prior to this study, Khurana et al. (2007) had shown that there is a good correlation between the position of the OCFB and the boundary of Ganymede's polar cap, suggesting that this is evidence of the effect of charged particles impacting the moon's surface. Khurana et al. (2007) suggested also that the equatorial leading/trailing asymmetry was due to the preferential flux of ions. Sputtering can remove part of the surface upper layers allowing the underlying fresh ice to emerge and be subsequently released in the exosphere. So,

583 the related redistribution of water frost on the surface (due to sputtering and also water deposition
584 from the exosphere) is expected to cause a surface brightening that is well correlated with the ion
585 precipitation patterns and the sputtered-H_2O water exosphere. Moreover, radiation can also have an
586 impact on the structure of surface water ice: indeed, the existence of amorphous ice –mostly in the
587 first micrometer layers is due to higher radiation processing (Hansen and McCord, 2004; 720 Famà
588 et al. 2010). Therefore, observing with MAJIS the surface regions that are expected to be mostly
589 bombarded by Jupiter's magnetospheric ions should provide also an indication of the expected water
590 deposition from the exosphere itself. Moreover, almost simultaneous observations of Ganymede's
591 exosphere and surface with MAJIS could allow to infer about the link between them in terms of water
592 deposition, especially if performed at different locations.
593
594 **4. Possible detectability of Ganymede's plumes**
595
596 Currently, there is no empirical evidence for the presence of plumes at Ganymede. However, lessons
597 learned from both Enceladus, where active plumes have been imaged by the ISS camera and the
598 VIMS spectrometer on board the Cassini spacecraft (Porco et al., 2006; Hedman, 2009), and Europa
599 (Roth et al., 2014; Sparks et al., 2016; Jia et al., 2018; Paganini et al., 2019), provide a good
600 motivation for estimating the plume detection capability at Ganymede by the instruments on board
601 JUICE.
602
603 In principle, MAJIS (as the JANUS camera) can detect plumes through the scattering of solar light
604 by plume grains. In the range of grain size inferred at Enceladus (radii of about 2-5 μm), the scattering
605 efficiency is strongly peaked in the forward direction, making the detection of plumes much more
606 likely in high solar phase angle configurations. Therefore, optimal conditions for plume detection
607 with MAJIS are the limb viewings at high phase angle and with a spatial resolution high enough to
608 resolve the plume in its vertical extension. In both Enceladus and Europa cases, plume heights have

609 been estimated to be of the order of 100-200 km (e.g., Roth et al., 2014) and this scale length is
610 assumed as an upper limit on Ganymede.
611
612 On the basis of the currently planned trajectories of spacecraft, the above mentioned observing
613 constraints are expected to be achieved several times along the JUICE mission, during Ganymede
614 flybys as well as during the Ganymede orbital phase. The different opportunities mainly differ in the
615 observing range, varying from $2 \cdot 10^5$ km to 4000 km, yielding large variations of spatial resolution.
616 We show here the evaluation of the detection limits on the plume density in three different
617 configurations of MAJIS observations, taken as study cases: (a) a distant flyby, (b) a close flyby, and
618 (c) a high orbit (GCO-5000). We point out that currently only case (c) is compatible with Sun
619 avoidance rules except when JUICE is in the shadow of Jupiter (and Ganymede is not), nevertheless,
620 with the scope to present better our methodology within the current paper, we speculate on all three
621 hypothetical cases.
622
623 In all cases, plume scattering properties are calculated using the Mie theory for spherical
624 homogeneous particles (Bohren and Huffman, 1983), assuming a pure water ice composition, and
625 grain sizes lognormally distributed with a 3 μm effective radius and a 1.5 effective variance. The
626 solar radiance scattered by the plume is evaluated in a single scattering approximation as

627 $$I_{pl}(\lambda) = \frac{1}{4\pi} F_{sun}(\lambda) \underline{C_{sca}}(\lambda) \underline{P}(\lambda, \alpha) N_{pl} f_f \quad (5)$$

628
629 being $F_{sun}(\lambda)$ the solar radiance at the actual heliocentric range, $\underline{C_{sca}}(\lambda)$ and $\underline{P}(\lambda, \alpha)$ respectively the
630 single scattering cross section and single scattering phase function of the plume particles, averaged
631 over their size distribution, N_{pl} the plume number column density, and f_f the filling factor of the
632 MAJIS pixel. The latter is computed as the fraction of the MAJIS instantaneous field-of-view
633 intersecting a cylindrical homogeneous plume, 200 km in height and 10 km in diameter. With this

assumption the filling factor equals unity for observing distances less than about 65000 km. Plume particles thermal emission intensity is estimated below 1% of the solar scattered radiation levels for wavelengths shortward of 5 μm (assuming a 120 K grain temperature), and is therefore neglected. Expected noise levels for plume observations, taking into account the source, background, and dark current noise sources assuming a detector temperature of 130 K for the MAJIS VIS-NIR channel (see Table 2), are evaluated as a function of the plume column density (in the line-of-sight direction) and exposure times. The resulting SNR appears higher in the 0.8-1.0 μm wavelength range, and the average SNR value in that range is used to define plume detection limits.

The results for the three study cases here considered are shown in Figure 7, for a range of MAJIS exposure times (no despiking processing included) and plume column densities, while the corresponding observing parameters are summarized in Table 4. The red, orange, and green thick lines indicate the column density detectable with a SNR level of 1, 2, or 3 respectively. For comparison, the range of plume densities estimated for the Enceladus case (Porco et al., 2006) are indicated by the blue-filled region.

Our analysis shows that the b) case (close flyby) is the most favorable one, since the simultaneous optimization of both resolution and phase angle enables the detection of low density plumes, 1-2 orders of magnitudes thinner than Enceladus ones, even with short integration times. In the a) case (distant flyby) the increase of observing distance pertaining to high phase angles makes the plume subpixel, and detection of thin features requires integration times longer than about 10 sec. The c) case (high-altitude orbit phase) appears the worst one, since even the detection of a high-density (Enceladus-like) plume requires very long integration times. It is interesting to note that the lower detection probability in the c) case is due to the smaller phase angle achievable in the orbit phase, which are predicted to not overcome the 140° value. A better performance may be achieved in this phase if the plume contains a significant population of submicron grains, whose forward scattering peak is less pronounced.

660 It is worth stressing that these estimations are based on the currently available radiometric model of
661 the instrumental response, while more quantitative predictions require the actual instrumental
662 response which will be measured after the integration of the MAJIS flight-model.
663

Table 4: Detectability of Ganymede plumes: parameters used for detection limits estimations for the three hypothetical study cases

Study case	S/c distance	Solar phase angle	Heliocentric distance	Spatial resolution	Filling factor for MAJIS pixel
a) distant flyby case (Dec. 2030)	189000 km	174°	5.33 AU	28 km/pixel	0.35
b) close flyby case (Sep. 2030)	4500 km	175°	5.37 AU	0.7 km/pixel	1.0
c) high orbit case (Nov. 2032)	7700 km	135°	5.10 AU	1.2 km/pixel	1.0

664
665

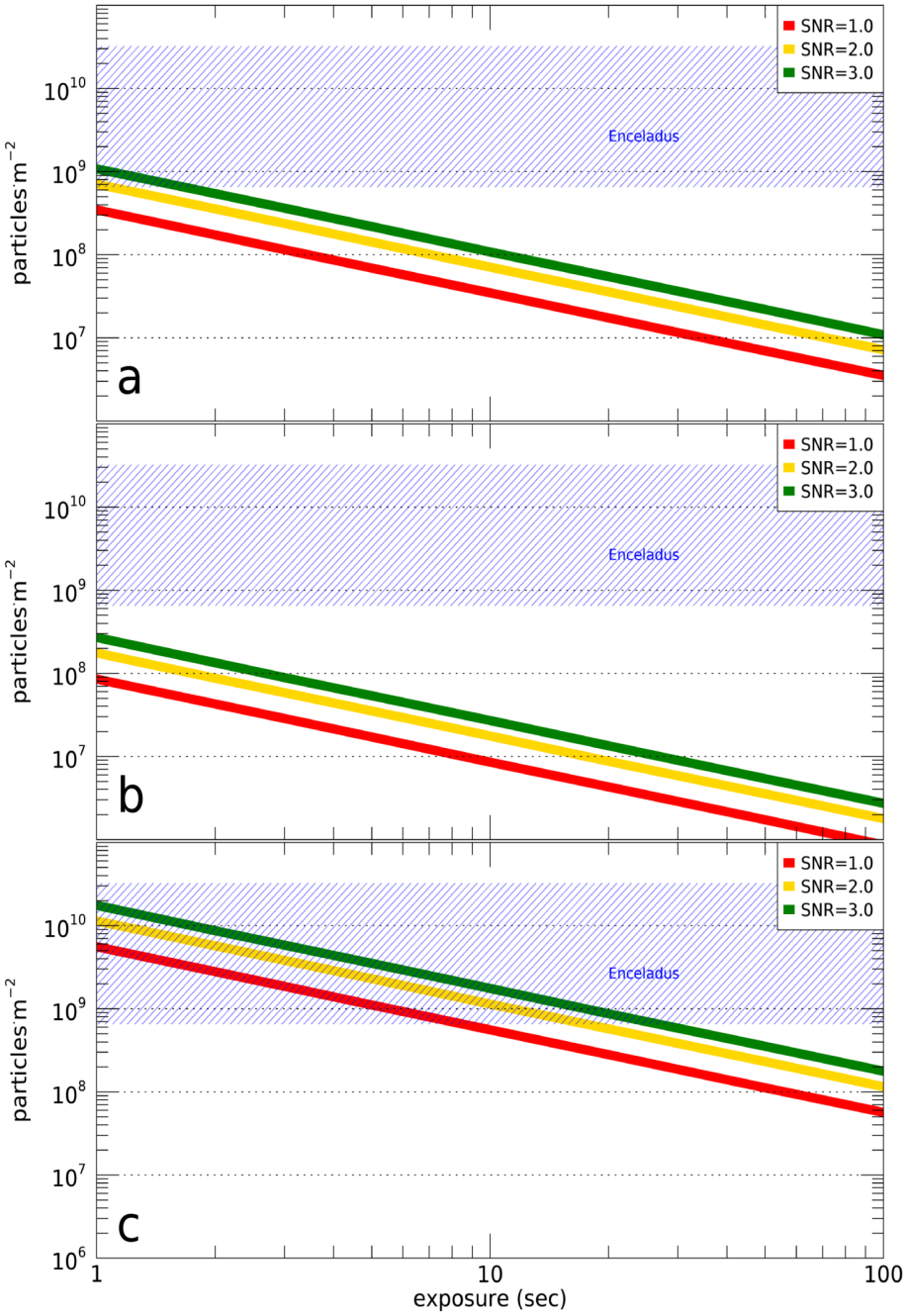

666

Figure 7: Detectability of a water ice plume in the three different study cases described in text and Table 4 and representing conditions encountered during different JUICE mission phases: distant flyby (panel a), close flyby (panel b), high orbit (panel c). Red, orange, and green lines indicate the plume column density detectable with SNR values of 1, 2, or 3, respectively (as average value in the 0.8-1.0 μm range). The blue-filled regions show the range of densities of the Enceladus plume. The despiking process has not been taken into account.

667

5. **Discussion and Conclusions**

Lunar exospheres are important sources of neutral gas in the outer Solar System often associated with the formation of torus-shaped clouds (e.g., Mauk et al., 2003; Shematovich, 2016). They play an important role in the balance between the neutral gas and magnetospheric plasma in the giant planetary systems. The determination of the properties of the exospheric environment provides the necessary information to better understand the weathering processes induced on ice by the radiation environment.

Surface sputtering and water sublimation play a key role in the generation and dynamical evolution of Ganymede's exosphere. In general, numerical models simulating the generation of Ganymede's surface-bounded H_2O exosphere agree that thermal ion populations provide a minor contribution to the total sputtering rate with respect to heavy energetic ions (e.g., Sulfur ions and Oxygen ions). Water sublimation is expected to be the dominant surface release process only locally, although some uncertainty in the considered rates exists due to the lack of quantitative information on the surface impurities concentration and actual temperature. For comparison, on Saturn's moon Tethys the intense bombardment of high-energy magnetospheric electrons collimated on the leading hemisphere of the moon is the driving mechanism causing the formation of the equatorial lens and nearby "Pacman" feature (Howett, 2012). As a consequence of the electrons bombardment, the ice grains displaced on the regolith are sinthered together (Filacchione et al., 2018), forming larger grains and causing local thermophysical anomalies: the lens appears in fact colder (Howett et al., 2012; Filacchione et al., 2016) and darker (Schenk et al., 2011; Filacchione et al., 2018) with respect to nearby regions not altered by the electron flux. Exospheric models for Ganymede (e.g., Marconi 2007; Turc et al., 2014; Plainaki et al., 2015; Shematovich 2016; Leblanc et al., 2017) generally almost agree in terms of water release rate from the surface and maximum H_2O vapor density, however, the different assumptions in each model result in different density profiles. Future

694 experimental work in estimating ice sputtering and radiolysis yields and even more accurate
695 estimations of the exosphere sources (e.g., through the consideration of the entire energy range of the
696 impinging ions) and loss rates (e.g., through the definition of the precise morphology of the plasma
697 around Ganymede) will certainly help to better estimate the vapor H_2O density distribution.
698
699 In this work, we provided a first evaluation of the potential of observing Ganymede's H_2O exosphere
700 with JUICE/MAJIS. Our main motivation for this exercise was the possibility to obtain IR radiation
701 measurements that will constrain the efficiency and morphology of the surface particle release as well
702 as the energy exchange between the Jovian system and the moon. Two representative observation
703 cases have been considered for observations from GCO-5000, one at high vertical resolution
704 (projected IFOV of ~1.1 km) and one at low vertical resolution (projected IFOV of ~10 km). The
705 results of our estimations provide evidence that given the specifications of MAJIS, the instrument has
706 the necessary sensitivity to observe the moon's water vapor environment with a SNR higher than 1
707 during limb observations with tangent altitude below 100 km from the surface and at latitudes ± 10°,
708 even when considering the model leading to the lowest column densities of water vapor. If current
709 exospheric models are correct, and in absence of plumes, we confirm that the H_2O exosphere to be
710 detected with MAJIS will be the one generated through water ice sublimation, since the SNR
711 corresponding to the sputtered water component is expected to be extremely low. Even if this were
712 the case, the possible investigation of Ganymede's exosphere with MAJIS is still important since it
713 can provide useful information for speculating on the surface weathering processes. We note that the
714 deposition of neutral species from the exosphere onto the moon's surface can spectrally mask the
715 weathering products or directly start new chemical patterns. Therefore, to understand the processes
716 of weathering we need first to characterize the moon's exosphere, even if only locally. Based on the
717 above, the most favorable observation condition during JUICE is the one focused on the region
718 around the subsolar point. For limb observations, MAJIS would require setting its slit tangent to the
719 limb, a configuration that avoids saturation from the satellite if the limb is sunlit, providing at the

same time optimum vertical resolution with spatial binning. Potential joint-observations between MAJIS and UVS are likely to increase the scientific return from the observation of Ganymede's exosphere. We note here that the estimations in the current paper are likely to be revised in the next years also due to theoretical model updates hence our results provide a first indicative range for the expected exospheric measurements. The upcoming measurements with JUICE will provide proof of the most realistic scenario among the ones currently proposed for the exosphere of Ganymede.

Considering the potential detection of plumes at Ganymede (if any), we showed that particular combination of resolution and phase angle shall enable to optimize the MAJIS observation and resulting SNR of low density plumes. The simulation indicates that MAJIS can detect plumes of density 1-2 orders of magnitudes thinner than the Enceladus ones by optimizing the integration times and selecting the VISNIR channel. Further detailed work in this direction is strongly required to take into consideration the expected properties of a potential plume at Ganymede (considering also the role of the moon's orbit phase around Jupiter), as well as the real performances of the instrument after characterization, the validation of the despiking algorithm once in flight, and (during Ganymede encounters), the compatibility between the necessary (for the observations) phase angles and the Sun avoidance rules requested by MAJIS. Potential planning for a series of observations at different latitudes together with JANUS, as done in the past for Enceladus by ISS and VIMS onboard Cassini (Hedman et al., 2009) will help us to better understand the properties of plumes (if any) and, possibly, their variability in time. Future work in this direction is intended.

There are some drawbacks related to the estimations presented in this paper. First, the current study considers as inputs the outputs of numerical simulations hence the differences among the obtained calculations cannot be neither rigorously nor easily attributed to specific parameters within each model. Different theoretical models of the H_2O exosphere, and different configurations between Ganymede, Jupiter and the Sun may result in different exosphere morphologies (see, for example,

746 Leblanc et al., 2017) hence this study provides only a preliminary and rough estimation of the
747 expected measurement by MAJIS. Indeed, Ganymede's magnetosphere changes continuously due to
748 the moon's motion above and below the Jupiter plasma sheet but also due to the variation of the
749 plasma sheet properties itself. Recently, Vogt et al. (2017) found that Jupiter's current sheet current
750 density parameter varies by ~15–20% with respect to its average value. The exosphere is expected to
751 be influenced by such changes in terms of both generation and loss process efficiency. The study of
752 the variation of the exosphere due to variations of the space environment external to Ganymede
753 (planetary space weather) is an important requisite for future estimations of its detectability and for
754 optimizing the observational conditions. Second, all the exospheric models considered in this study
755 assume that the H_2O sublimation rate above the subsolar point is relatively high. Unfortunately, there
756 are currently no published observational evidences that prove (or deny) this fact. At a larger
757 perspective, future exploration of the Outer Solar System requires knowledge on the planetary space
758 weather conditions near and within the system under investigation (for a more detailed discussion in
759 this context see Plainaki et al. (2016) and references therein). Last, our estimations show that the
760 dominant component to be observed with MAJIS is likely sublimated H_2O, for which all models
761 estimate the same maximum concentration. Although the sputtered H_2O exosphere, as estimated
762 nowadays by models, is likely under the detectability limits of MAJIS, the remote possibility of its
763 observation should not be ruled out. This is because ongoing laboratory work on the efficiency of
764 H_2O release from ice as well as recent estimations of updated release yields (see, for instance, Teolis
765 et al. 2017) and of the role of the radiation environment (see, for instance, Poppe et al. 2018) and
766 secondary sputtering (Carnielli et al., 2019) may result in an increase of the H_2O density. In such a
767 case, the current estimations provide only a lower limit for future detection.
768
769 To accurately estimate the SNR expected for MAJIS during limb observations of Ganymede's H_2O
770 exosphere, further detailed work is required, taking also into consideration further opportunities to
771 observe the exosphere of Ganymede. The current study, therefore, will be expanded and the results

772 will be integrated considering different observational opportunities during the JUICE mission. In
773 particular, we plan to integrate in our radiance simulator the actual MAJIS observational geometries
774 (incidence and emission angles, tangent altitudes, spacecraft distances, etc.) based on the
775 Consolidated Report on Mission Analysis (CReMA; Boutonnet and Schoenmaekers, 2012)
776 trajectories and the instrument pointing abilities. Such an approach will provide feedback for driving
777 the MAJIS observational planning in order to optimize the Ganymede's exosphere detection
778 accordingly with the MAJIS spectral sensitivity.
779
780 **References**
781
782 Bagenal, F., Wilson, R. J., Siler, S., Paterson, W. R. et al., 2016. Survey of Galileo plasma
783 observations in Jupiter's plasma sheet. Journal of Geophysical Research: Planets, 121, 871–894. DOI:
784 10.1002/2016JE005009
785 Bahr, D. A., Famá, M., Vidal, R. A., & Baragiola, R. A., 2001. Radiolysis of water ice in the
786 outer solar system: Sputtering and trapping of radiation products. Journal of Geophysical Research,
787 106(E12), 33,285–33,290, DOI: 10.1029/2000JE001324
788 Barth C.A., Hord, C.W., Stewart, A.I.F., et al. (1996). Galileo ultraviolet spectrometer
789 observations of atomic hydrogen in the atmosphere if Ganymede. Geophys. Res. Lett., 24, 2147-
790 2150.
791 Bockelée-Morvan, D., 1987. A model for the excitation of water in comets. Astronomy and
792 Astrophysics, 181, 1, 169-181, 1987A&A., 181..169B
793 Bockelée-Morvan, D., Crovisier, J., Mumma, M. J., and Weaver, H. A., 2004. The composition
794 of cometary volatiles, in: M. C. Festou, H. U. Keller, & H. Weaver (Eds), Comets II, 391
795 Bockelée-Morvan, D., Crovisier, J., Erard, S., Capaccioni, F. et al., 2016. Evolution of CO_2,
796 CH_4, and OCS abundances relative to H_2O in the coma of comet 67P around perihelion from

797 *Rosetta*/VIRTIS-H observations, *Monthly Notices of the Royal Astronomical Society*, 462, Suppl_1,
798 S170–S183, DOI: 10.1093/mnras/stw2428
799 Bohren C. F., Huffman D. R., 1983. Absorption and Scattering of Light by Small Particles.
800 Wiley, New York
801 Boutonnet, A., Schoenmaekers, J.: JUICE: Consolidated Report on Mission Analysis (CReMA
802), ESA, 2012
803 Broadfoot A. L., Belton M. J., Takacs P. Z., Sandel B. R. et al., 1979. Extreme ultraviolet
804 observations from Voyager 1 encounter with Jupiter. Science, 204:979–982,
805 DOI:10.1126/science.204.4396.979
806 Coustenis, A., Atreya, S., Castillo, J., Coll, P., 2010. Surfaces and atmospheres of the outer
807 planets, their satellites and ring systems: Part VI , Planetary and Space Science, 58, 13, 1665-1666,
808 DOI: 10.1016/j.pss.2010.09.00
809 Crovisier, J., 1987. Rotational and vibrational synthetic spectra of linear parent molecules in
810 comets, Astronomy and Astrophysics Supplement Series (ISSN 0365-0138), 68, 2, 223-258,
811 Bibcode: 1987A&AS...68..223C
812 Famà, M., Shi, J., Baragiola, R.A., 2008. Sputtering of ice by low-energy ions. Surf. Sci.
813 602, 156–161, DOI: 10.1016/j.susc.2007.10.002
814 Fatemi, S., Poppe, A. R., Khurana, K. K., Holmström, M. et al., 2016. On the formation of
815 Ganymede's surface brightness asymmetries: Kinetic simulations of Ganymede's magnetosphere.
816 Geophysical Research Letters, 43, 4745–4754, DOI: 10.1002/2016GL068363
817 Feldman, P.D., McGrath, M.A., Strobel, D.F., Moos, H.W., Retherford, K.D., Wolven, B.C.,
818 2000. HST/STIS ultraviolet imaging of polar Aurora on Ganymede, Astrophys. J., 535, 1085–1090,
819 DOI: 10.1086/308889.
820 Filacchione, G., D'Aversa, E., Capaccioni, F., Clark, R.N. et al. (2016). Saturn's icy satellites
821 investigated by Cassini-VIMS. IV. Daytime temperature maps. Icarus, 271, 292–313, DOI:
822 10.1016/j.icarus.2016.02.019

823 Filacchione, G., Ciarniello, M., D'Aversa, E., Capaccioni, F. et al., 2018. Photometric modeling
824 and VIS-IR Albedo maps of Tethys from Cassini-VIMS. Geophysical Research Letters, 45, 6400–
825 6407, DOI: 10.1029/2018GL078602.
826 Gordon, I.E., Rothman, L.S., Hill, C., Kochanov, R.V. et al., 2017. The HITRAN2016 molecular
827 spectroscopic database, Journal of Quantitative Spectroscopy and Radiative Transfer, 203, 3-69, DOI:
828 10.1016/j.jqsrt.2017.06.038
829 Grasset, O., Dougherty, M.K., Coustenis, A., Bunce, E.J., et al., 2013. JUpiter Icy moons
830 Explorer (JUICE): an ESA mission to orbit Ganymede and to characterize the Jupiter system. Planet.
831 Space Sci., 78,1–21, DOI: 10.1016/j.pss.2012.12.002
832 Guerri, I., Fabbri, A., Tommasi, L., Taiti, A. et al., 2018. The optical design of the MAJIS
833 instrument on board of the JUICE mission, Proc. SPIE 10690, Optical Design and Engineering VII,
834 106901L (5 June 2018), doi:10.1117/12.2312013
835 Gurnett, D.A., Kurth, W.S., Roux, A., Bolton, S.J., Kennel, C.F., 1996. Evidence for a
836 magnetosphere at Ganymede from plasma-wave observations by the Galileo spacecraft. Nature, 384,
837 535–537, DOI: 10.1038/384535a0.
838 Hall, D.T., Feldman, P.D., McGrath, M.A., Strobel, D.F., 1998. The far-ultraviolet oxygen
839 airglow of Europa and Ganymede. Astrophys. J., 499, 475–481, DOI: 10.1086/305604
840 Hartogh et al., 2013
841 http://herschel.esac.esa.int/TheUniverseExploredByHerschel/presentations/13a-
842 1720_HartoghP.pdf
843 Hedman, M.M., Nicholson, P.D., Showalter, M.R., Brown, R.H., Buratti, B.J., Clark, R.N. 2009.
844 Spectral observations of the Enceladus plume with Cassini-VIMS. ApJ, 693, 1749-1762, DOI:
845 10.1088/0004-637X/693/2/1749
846 Howett, C. J. A., Spencer, J. R., Hurford, T., Verbiscer, A., & Segura, M. (2012). PacMan
847 returns: An electron-generated thermal anomaly on Tethys. Icarus, 221, 1084–1088, DOI:
848 10.1016/j.icarus.2012.10.013

Jia, X., Walker, R.J., Kivelson, M.G., Khurana,K.K., Linker, J.A., 2008. Three-dimensional MHD simulations of Ganymede's magnetosphere. J. Geophys. Res. Space Physics, 113, A06212, DOI: 10.1029/2007JA012748.

Jia, X., Walker, R.J., Kivelson, M.G.,Khurana, K.K., Linker, J.A., 2009. Properties of Ganymede's magnetosphere inferred from improved three-dimensional MHD simulations. J. Geophys. Res. Space Physics, 114, A09209, DOI: 10.1029/2009JA014375.

Jia, X., Kivelson, M.G., Khurana, K.K., Kurth, W.S. 2018. Evidence of a plume on Europa from Galileo magnetic and plasma wave signatures. Nature Astronomy, 2, 459–464, DOI: 10.1038/s41550-018-0450-z

Johnson, R. E., 1990. Interactions with surfaces. Energetic charged-particle interactions with atmospheres and surfaces (pp. 75–135). Berlin: Springer-Verlag

Khurana, K. K., Pappalardo, R. T., Murphy, N., & Denk, T., 2007. The origin of Ganymede's polar caps. Icarus, 191, 193–202, DOI: 10.1016/j.icarus.2007.04.022

Kivelson, M. G., Bagenal, F., Kurth, W. S., Neubauer, F. M., Paranicas, C., & Saur, J. (2004). Magnetospheric interactions with satellites, Jupiter: The planet, satellites, and magnetosphere (pp. 513–536). Cambridge, UK: Cambridge University Press.

Kivelson, M. G., Khurana, K. K., Russell, C. T., Walker, R. J. et al., 1996. Discovery of Ganymede's magnetic field by the Galileo spacecraft. Nature 384, 537–541, DOI: 10.1038/384537a0

Kivelson, M.G. ,Khurana, K.K., Coroniti, F.V., Joy, S. et al., 1997. Magnetic field and magnetosphere of Ganymede. Geophys. Res. Lett. 24, 2155, DOI: 10.1029/97GL02201

Langevin, Y., Piccioni, G., Filacchione, G., Poulet, F. & Dumesnil, C., 2018. MAJIS, the VIS-IR imaging spectrometer of JUICE, IPM 2018, E1.

Langevin, Y., Piccioni, G. and the MAJIS Team, 2017. The MAJIS visible/NIR imaging spectrometer on board the ESA JUICE mission : updated design, implications for performances and science goals, EPSC2017-931.

874 Leblanc, F., Oza, A.V., Leclercq, L., Schmidt, C. et al. 2017. On the orbital variability of
875 Ganymede's atmosphere, Icarus, 293, 185-198, DOI: 10.1016/j.icarus.2017.04.025
876 Ligier, N., Paranicas, C., Carter, J., et al. 2019. Surface composition and properties of Ganymede:
877 Updates from ground-based observations with the near-infrared imaging spectrometer
878 SINFONI/VLT/ESO, Icarus, 333, 496, DOI:10.1016/j.icarus.2019.06.013
879 Lucchetti, A., Plainaki, C., Cremonese, G., Milillo, A. et al. 2016. Loss rates of Europa's
880 exosphere, PSS, 130, 14–23, doi:10.1016/j.pss.2016.01.009
881 Marconi, M.L., 2007. A kinetic model of Ganymede's atmosphere. Icarus, 190, 155–174, DOI:
882 10.1016/j.icarus.2007.02.016
883 Moore, M. H., Hudson, R. L., Carlson, R.W., 2007. The radiolysis of SO2 and H2S in water ice:
884 Implications for the icy Jovian satellites. Icarus, 189, 409–423, DOI: 10.1016/j.icarus.2007.01.018
885 Orton, G.S., Spencer, J.R., Travis, L.D., Martin, T.Z. et al. 1996. Galileo photopolarimeter–
886 radiometer observations of Jupiter and the Galilean satellites. Science 274, 389–392.
887 Paganini, L., Villanueva, G.L., Roth, L., Mandell, A.M., Hurford, T.A. et al. 2019. A
888 measurement of water vapour amid a largely quiescent environment on Europa, Nature Astronomy,
889 DOI: 10.1038/s41550-019-0933-6
890 Paranicas, C., Paterson, W.R., Cheng, A.F., Mauk, B.H. et al., 1999. Energetic particle
891 observations near Ganymede., J. Geophys. Res. 104, 17459–17470, DOI: 10.1029/1999JA900199.
892 Piccioni, G., Langevin, Y., Filacchione, G., Poulet, F. et al., 2014. MAJIS, the Moons And Jupiter
893 Imaging Spectrometer, designed for the future ESA/JUICE mission, EGU General Assembly
894 Conference Abstracts, 16, 10925.
895 Piccioni, G., Tommasi, L., Langevin, Y., Filacchione, G., et al., 2019. Scientific goals and
896 technical challenges of the MAJIS imaging spectrometer for the JUICE mission. Proceedings of the
897 2019 IEEE 5th International Workshop on Metrology for AeroSpace, Turin (Italy), 19-21 June 2019.
898 DOI: 10.1109/MetroAeroSpace.2019.8869566.

899 Plainaki, C., Milillo, A., Mura, A., Orsini, S. et al., 2010. Neutral particle release from Europa's
900 surface. Icarus 210, 385–395, DOI: 10.1016/j.icarus.2010.06.041
901 Plainaki, C., A. Milillo, A. Mura, S. Orsini, S. et al., 2012. The role of sputtering and radiolysis
902 in the generation of Europa exosphere. Icarus, 218, 2, 956–966, DOI: 10.1016/j.icarus.2012.01.023
903 Plainaki, C., Milillo, A., Mura, A., Saur, J. et al., 2013. Exospheric O2 densities at Europa
904 during different orbital phases, Planet. Space Sci., 88, 42, DOI: 10.1016/j.pss.2013.08.011
905 Plainaki, C., Milillo, A., Massetti, S., Mura, A. et al., 2015. The H2O and O2 exospheres of
906 Ganymede: the result of a complex interaction between the Jovian magnetospheric ions and the icy
907 moon. Icarus, 245, 306–319, DOI: 10.1016/j.icarus.2014.09.018
908 Plainaki, C., Lilensten, J., Radioti, A., Andriopoulou,M. et al., 2016. Planetary space weather:
909 scientific aspects and future perspectives, J. Space Weather Space Clim., 6, A31, 2016, DOI:
910 10.1051/swsc/2016024
911 Plainaki, C., Cassidy, T.A., Shematovich, V.I., Milillo, A. et al., 2018. Towards a Global Unified
912 Model of Europa's Tenuous Atmosphere, Space Sci Rev, 214: 40, DOI: 10.1007/s11214-018-0469-6
913 Poppe, A. R., Fatemi, S., Khurana, K.K., 2018. Thermal and energetic ion dynamics in
914 Ganymede's magnetosphere. Journal of Geophysical Research: Space Physics, 123, 4614–4637,
915 DOI: 10.1029/2018JA025312
916 Porco, C.C., Helfenstein, P., Thomas, P.C., Ingersoll, A.P. et al., 2006. Cassini observes the
917 active south pole of Enceladus, Science,311,1393-1401, DOI: 10.1126/science.1123013
918 Roth, L., Saur, J., Retherford, K.D., Strobel, D.F. et al., 2014. Transient Water Vapor at Europa's
919 South Pole, Science, 343, 171-174, doi: 10.1126/science.1247051
920 Schenk, P., Hamilton, D. P., Johnson, R. E., McKinnon, W. B. et al., 2011. Plasma, plumes and
921 rings: Saturn system dynamics as recorded in global color patterns on its midsize icy satellites. Icarus,
922 211, 740–757, DOI: 10.1016/j.icarus.2010.08.016
923 Shematovich, V.I., 2016. Neutral atmosphere near the icy surface of Jupiter's moon Ganymede,
924 Solar System Research, 50, 4, 262–280, DOI: 10.1134/S0038094616040067

925 Smith, B. A., Soderblom, L. A., Beebe, R., Boyce, J. et al., 1979. The Galilean satellites and
926 Jupiter: Voyager 2 Imaging Science results, Science, 206(4421), 927–950
927 Sparks, W. B., Hand, K. P., McGrath, M.A., Bergeron, E. et al., 2016. Probing for evidence of
928 plumes on Europa with HST/STIS. Astrophys.Journ., 829,121, DOI: 10.3847/0004-637X/829/2/121
929 Sparks, W. B. et al. 2017. Active Cryovolcanism on Europa? ApJL 839 L18., DOI:
930 10.3847/2041-8213/aa67f8
931 Teolis, B. D., Loeffler, M. J., Raut, U., Famá, M. et al., 2006. Ozone synthesis on the icy
932 satellites. The Astrophysical Journal, 644, L141–L144.
933 Teolis, B. D., Plainaki, C., Cassidy, T. A., Raut, U., 2017. Water ice radiolytic O2, H2, and H2O2
934 yields for any projectile species, energy, or temperature: A model for icy astrophysical bodies. Journal
935 of Geophysical Research: Planets, 122, 1996–2012, DOI: 10.1002/2017JE005285
936 Turc, L., Leclercq, L., Leblanc, F., Modolo, R. et al., 2014. Modelling Ganymede's neutral
937 environment: A 3D test-particle simulation, Icarus, 229, 157–169, DOI: 10.1016/j.icarus.2013.11.005
938 Villanueva G. L., Mumma M. J., Bonev B. P., Novak R.E. et al., 2012. Water in planetary and
939 cometary atmospheres: H2O/HDOtransmittance and fluorescence models, J. Quant. Spectrosc.
940 Radiat. Transf., 113, 202, DOI: 10.1016/j.jqsrt.2011.11.001
941 Vogt, M.F., Bunce, E.J., Nichols, J.D., Clarke, J.T. et al., 2017. Long-term variability of
942 Jupiter's magnetodisk and implications for the aurora, Journal of Geophysical Research: Space
943 Physics, 122, 12,090–12,110, DOI: 10.1002/2017JA024066
944 Williams, D.J., Mauk, B.H., McEntire, R.W., Roelof, E.C. et al., 1997. Energetic particle
945 signatures at Ganymede: Implications for Ganymede's magnetic field. Geophysical Research Letters,
946 24(17), 2163–2166
947 Williams, D.J., 2001. Ganymede's ionic radiation belts. Geophysical Research Letters, 28(19),
948 3793–3796
949 Williams, D. J., McEntire, R. W., Jaskulek, S., & Wilken, B. (1992). The Galileo energetic
950 particles detector. Space Science Reviews, 60, 385–412.

APPENDIX

Figure A1: Simulated MAJIS spectrum (black line) of the H_2O Non-LTE emission between 2.4 and 3 μm for Ganymede's exosphere model by Marconi et al. (2007) at lat~10°N and tangent altitudes of 1, 10, 20, 50, 100 km above the surface, from top to bottom panel respectively. Red line indicates the predicted Noise Equivalent Spectral Radiance (NESR) of the MAJIS instrument for high vertical resolution observations.

Figure A2: Simulated MAJIS spectrum (black line) of the H_2O Non-LTE emission between 2.4 and 3 μm for Ganymede's exosphere model by Shematovich et al. (2016) at lat~10°N and tangent altitudes of 1, 10, 20, 50, 100 km above the surface, from top to bottom panel respectively. Red line indicates the predicted Noise Equivalent Spectral Radiance (NESR) of the MAJIS instrument for high vertical resolution observations.

Figure A3: Simulated MAJIS spectrum (black line) of the H_2O Non-LTE emission between 2.4 and 3 μm for Ganymede's exosphere model by Turc et al. (2014) at lat~10°N and tangent altitudes of 1, 10, 20, 50, 100 km above the surface, from top to bottom panel respectively. Red line indicates the predicted Noise Equivalent Spectral Radiance (NESR) of the MAJIS instrument for high vertical resolution observations.

Figure A1

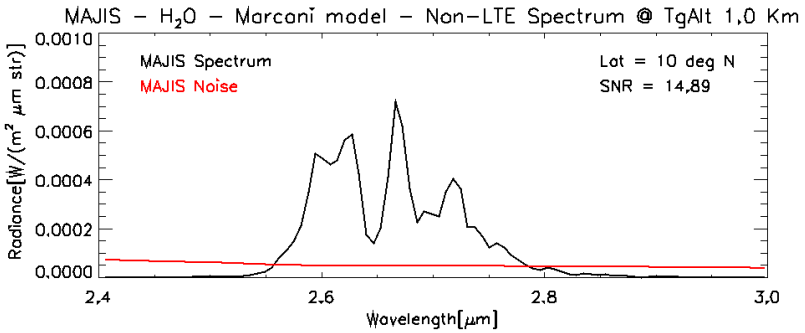

978

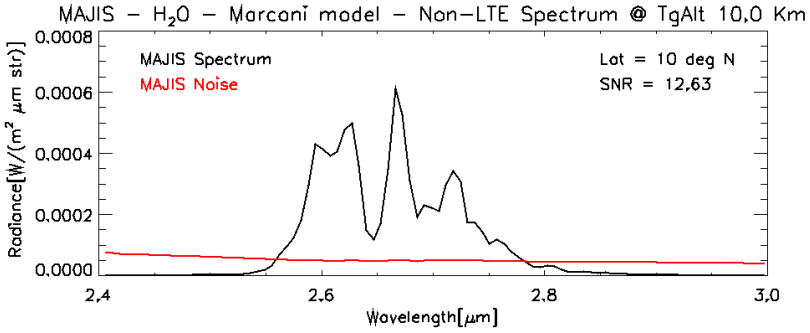

979

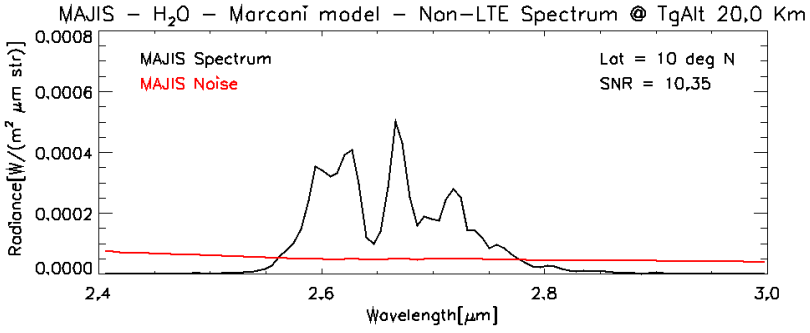

980

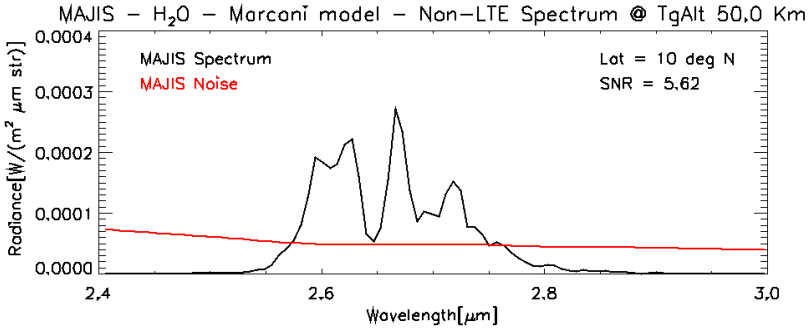

981

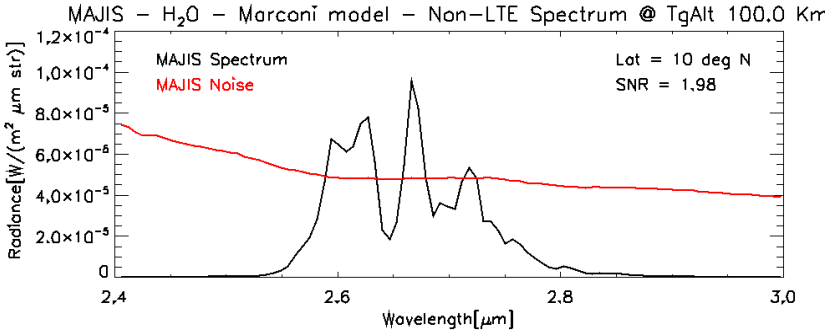

982

Figure A2

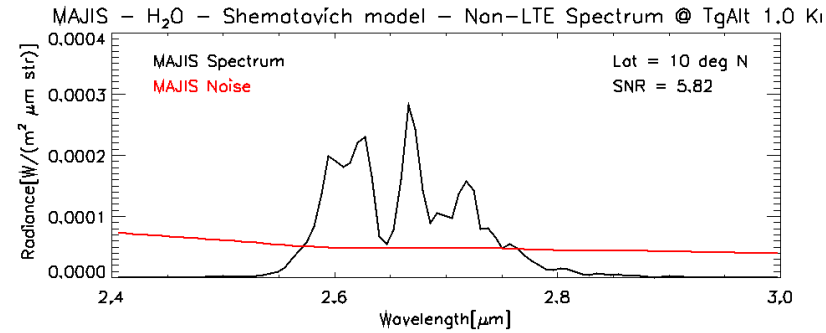

983

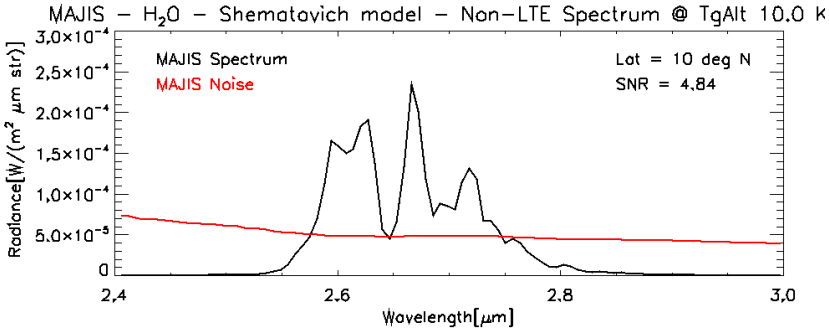

984

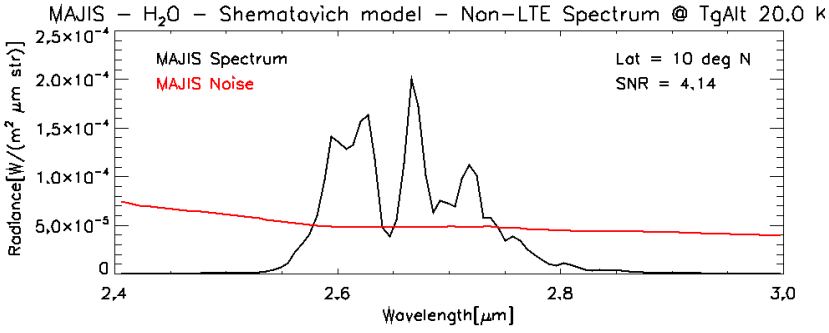

985

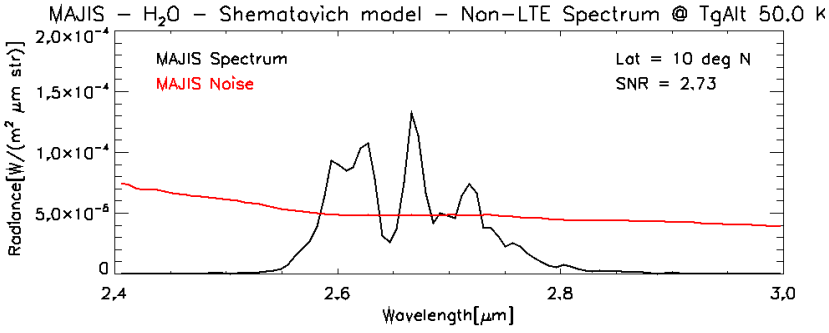

986

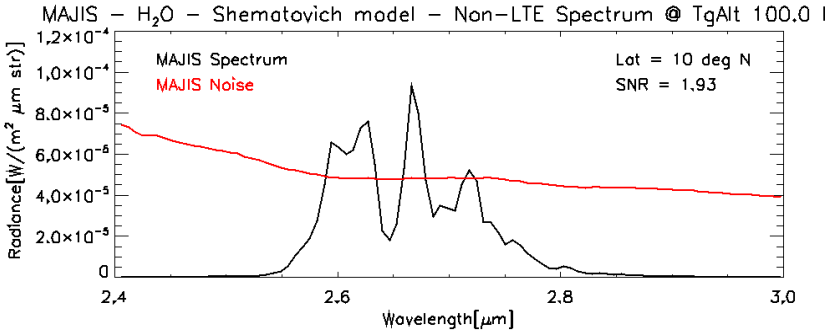

987

Figure A3

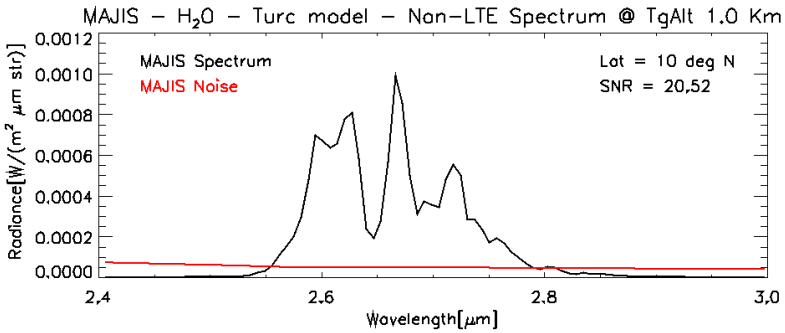

988

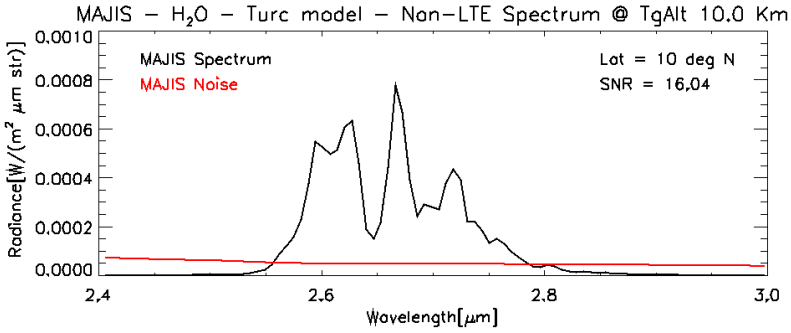

989

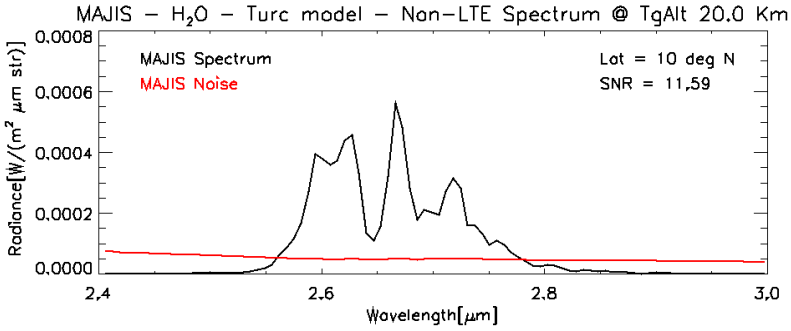

990

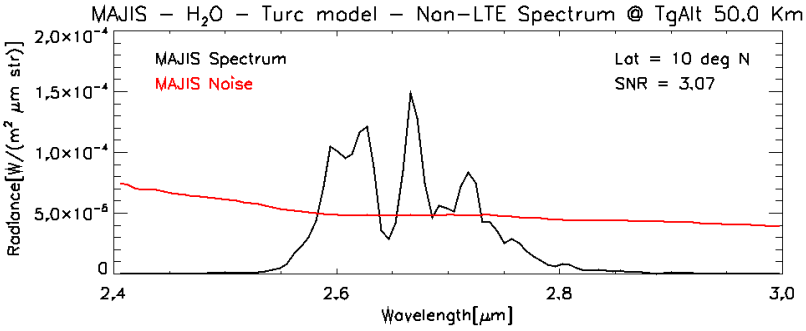

991

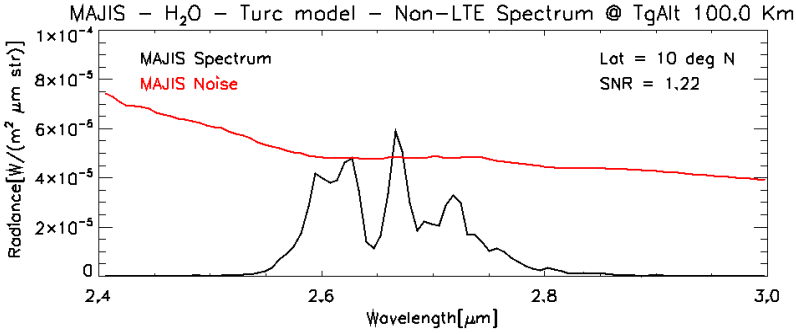

992